



Prospects for Cherenkov Telescope Array Observations of the Young Supernova Remnant RX J1713.7–3946

F. Acero¹, R. Aloisio^{2,3}, J. Amans⁴, E. Amato², L. A. Antonelli⁵, C. Aramo⁶, T. Armstrong⁷, F. Arqueros⁸, K. Asano⁹, M. Ashley¹⁰, M. Backes¹¹, C. Balazs¹², A. Balzer¹³, A. Bamba^{14,15}, M. Barkov¹⁶, J. A. Barrio⁸, W. Benbow¹⁷, K. Bernlöhr¹⁸, V. Beshley¹⁹, C. Bigongiari²⁰, A. Biland²¹, A. Bilinsky²², E. Bissaldi²³, J. Biteau²⁴, O. Blanch²⁵, P. Blasi², J. Blazek²⁶, C. Boisson⁴, G. Bonanno²⁷, A. Bonardi²⁸, C. Bonavolontà⁶, G. Bonnoli²⁹, C. Braiding¹⁰, S. Brau-Nogué³⁰, J. Bregeon³¹, A. M. Brown⁷, V. Bugaev³², A. Bulgarelli³³, T. Bulik³⁴, M. Burton¹⁰, A. Burtovoi³⁵, G. Busetto³⁶, M. Böttcher³⁷, R. Cameron³⁸, M. Capalbi³⁹, A. Caproni⁴⁰, P. Caraveo⁴¹, R. Carosi⁴², E. Cascone²⁹, M. Cerruti¹⁷, S. Chaty¹, A. Chen⁴³, X. Chen⁴⁴, M. Chernyakova⁴⁵, M. Chikawa⁴⁶, J. Chudoba²⁶, J. Cohen-Tanugi³¹, S. Colafrancesco⁴³, V. Conforti³³, J. L. Contreras⁸, A. Costa²⁷, G. Cotter⁴⁷, S. Covino²⁹, G. Covone⁶, P. Cumani²⁵, G. Cusumano³⁹, F. D’Ammando⁴⁸, D. D’Urso⁴⁹, M. Daniel¹⁷, F. Dazzi⁵⁰, A. De Angelis³⁶, G. De Cesare³³, A. De Franco⁴⁷, F. De Frondat⁴, E. M. de Gouveia Dal Pino⁵¹, C. De Lisio⁶, R. de los Reyes Lopez¹⁸, B. De Lotto⁵², M. de Naurois⁵³, F. De Palma⁵⁴, M. Del Santo³⁹, C. Delgado⁵⁵, D. della Volpe⁵⁶, T. Di Girolamo⁶, C. Di Giulio⁵⁷, F. Di Pierro⁵⁸, L. Di Venere⁵⁹, M. Doro³⁶, J. Dournaux⁴, D. Dumas⁴, V. Dworkadas⁶⁰, C. Díaz⁵⁵, J. Ebr²⁶, K. Egberts⁶¹, S. Einecke⁶², D. Elsässer⁶³, S. Eschbach⁶⁴, D. Falceta-Goncalves⁶⁵, G. Fasola⁴, E. Fedorova⁶⁶, A. Fernández-Barral²⁵, G. Ferrand¹⁶, M. Fesquet⁶⁷, E. Fiandrini⁴⁹, A. Fiasson⁶⁸, M. D. Filipović⁶⁹, V. Fioretti³³, L. Font⁷⁰, G. Fontaine⁵³, F. J. Franco⁷¹, L. Freixas Coromina⁵⁵, Y. Fujita⁷², Y. Fukui⁷³, S. Funk⁶⁴, A. Förster¹⁸, A. Gadola⁷⁴, R. Garcia López⁷⁵, M. Garczarczyk⁷⁶, N. Giglietto²³, F. Giordano⁵⁹, A. Giuliani⁴¹, J. Glicenstein⁷⁷, R. Gnatyk⁶⁶, P. Goldoni⁷⁸, T. Grabarczyk⁷⁹, R. Graciani⁸⁰, J. Graham⁷, P. Grandi³³, J. Granot⁸¹, A. J. Green⁸², S. Griffiths²⁵, S. Gunji⁸³, H. Hakobyan⁸⁴, S. Hara⁸⁵, T. Hassan²⁵, M. Hayashida⁹, M. Heller⁵⁶, J. C. Helo⁸⁴, J. Hinton¹⁸, B. Hnatyk⁶⁶, J. Huet⁴, M. Huetten⁷⁶, T. B. Humensky⁸⁶, M. Hussein⁸⁷, J. Hörandel²⁸, Y. Ikeno⁸⁸, T. Inada⁹, Y. Inoue⁸⁹, S. Inoue¹⁶, T. Inoue⁹⁰, Y. Inoue⁹¹, K. Ioka⁹², M. Iori⁹³, J. Jacquemier⁶⁸, P. Janecek²⁶, D. Jankowsky⁶⁴, I. Jung⁶⁴, P. Kaaret⁹⁴, H. Katagiri⁹⁵, S. Kimeswenger⁹⁶, S. Kimura⁸⁸, J. Knödseder³⁰, B. Koch⁴⁴, J. Kocot⁷⁹, K. Kohri⁹⁷, N. Komin⁴³, Y. Konno⁹⁸, K. Kosack¹, S. Koyama⁹¹, M. Kraus⁶⁴, H. Kubo⁹⁸, G. Kukec Mezek⁹⁹, J. Kushida⁸⁸, N. La Palombara⁴¹, K. Lalik¹⁰⁰, G. Lamanna⁶⁸, H. Landt⁷, J. Lapington¹⁰¹, P. Laporte⁴, S. Lee⁹¹, J. Lees⁶⁸, J. Lefacheur⁴, J.-P. Lenain¹⁰², G. Leto²⁷, E. Lindfors¹⁰³, T. Lohse¹⁰⁴, S. Lombardi⁵, F. Longo¹⁰⁵, M. Lopez⁸, F. Lucarelli⁵, P. L. Luque-Escamilla¹⁰⁶, R. López-Coto²⁵, M. C. Maccarone³⁹, G. Maier⁷⁶, G. Malaguti³³, D. Mandat²⁶, G. Maneva¹⁰⁷, S. Mangano⁵⁵, A. Marcowith³¹, J. Martí¹⁰⁶, M. Martínez²⁵, G. Martínez⁵⁵, S. Masuda⁹⁸, G. Maurin⁶⁸, N. Macted¹⁰, C. Melioli⁵¹, T. Mineo³⁹, N. Mirabal⁸, T. Mizuno¹⁰⁸, R. Moderski¹⁰⁹, M. Mohammed¹¹⁰, T. Montaruli⁵⁶, A. Moralejo²⁵, K. Mori¹¹¹, G. Morlino³, A. Morselli⁵⁷, E. Moulin⁷⁷, R. Mukherjee⁸⁶, C. Mundell¹¹², H. Muraishi¹¹³, K. Murase⁹, S. Nagataki¹⁶, T. Nagayoshi¹¹⁴, T. Naito⁸⁵, D. Nakajima^{9,115}, T. Nakamori⁸³, R. Nemmen⁵¹, J. Niemiec¹⁰⁰, D. Nieto⁸⁶, M. Nieves-Rosillo⁸, M. Nikolajuk¹¹⁶, K. Nishijima⁸⁸, K. Noda^{9,115}, L. Noguez²⁵, D. Nosek¹¹⁷, B. Novosyadlyj²², S. Nozaki⁹⁸, Y. Ohira¹¹⁸, M. Ohishi⁹, S. Ohm⁷⁶, A. Okumura¹¹⁹, R. A. Ong¹²⁰, R. Orito¹²¹, A. Orlati⁴⁸, M. Ostrowski¹²², I. Oya⁷⁶, M. Padovani³¹, J. Palacio²⁵, M. Palatka²⁶, J. M. Paredes⁸⁰, S. Pavy⁵³, A. Pe’er¹¹⁵, M. Persic^{52,123}, P. Petrucci¹²⁴, O. Petruk¹⁹, A. Pisarski¹¹⁶, M. Pohl⁶¹, A. Porcelli⁵⁶, E. Prandini¹²⁵, J. Prast⁶⁸, G. Principe⁶⁴, M. Prouza²⁶, E. Pueschel¹²⁶, G. Pühlhofer¹²⁷, A. Quirrenbach¹¹⁰, M. Rameez⁵⁶, O. Reimer¹²⁸, M. Renaud³¹, M. Ribó⁸⁰, J. Rico²⁵, V. Rizi³, J. Rodriguez¹, G. Rodriguez Fernandez⁵⁷, J. J. Rodríguez Vázquez⁵⁵, P. Romano³⁹, G. Romeo²⁷, J. Rosado⁸, J. Roussele¹²⁰, G. Rowell¹²⁹, B. Rudak¹⁰⁹, I. Sadeh⁷⁶, S. Safi-Harb⁸⁷, T. Saito⁹⁸, N. Sakaki⁹, D. Sanchez⁶⁸, P. Sangiorgi³⁹, H. Sano⁷³, M. Santander⁸⁶, S. Sarkar⁴⁷, M. Sawada¹¹⁸, E. J. Schioppa⁵⁶, H. Schoorlemmer¹⁸, P. Schovaneck²⁶, F. Schussler⁷⁷, O. Sergijenko²², M. Servillat⁴, A. Shalchi⁸⁷, R. C. Shellard¹³⁰, H. Siejkowski⁷⁹, A. Sillanpää¹⁰³, D. Simone⁵⁴, V. Sliuser¹²⁵, H. Sol⁴, S. Stanić⁹⁹, R. Starling¹⁰¹, Ł. Stawarz¹²², S. Stefanik¹¹⁷, M. Stephan¹³, T. Stolarczyk¹, M. Szonecki¹³¹, T. Szeplieniec⁷⁹, G. Tagliaferri²⁹, H. Tajima¹¹⁹, M. Takahashi⁹, J. Takeda⁸³, M. Tanaka⁹⁷, S. Tanaka⁸⁹, L. A. Tejedor⁸, I. Telezhinsky⁶¹, P. Temnikov¹⁰⁷, Y. Terada¹¹⁴, D. Tesaro³⁶, M. Teshima^{9,115}, V. Testa⁵, S. Thoudam¹³², F. Tokanai⁸³, D. F. Torres¹³³, E. Torresi³³, G. Tosti²⁹, C. Townsley⁵⁰, P. Travnicek²⁶, C. Trichard¹³⁴, M. Trifoglio³³, S. Tsujimoto⁸⁸, V. Vagelli⁴⁹, P. Vallania²⁰, L. Valore⁶, W. van Driel⁴, C. van Eldik⁶⁴, J. Vandenbroucke¹³⁵, V. Vassiliev¹²⁰, M. Vecchi¹³⁶, S. Vercellone³⁹, S. Vergani⁴, C. Vigorito⁵⁸, S. Vorobiov⁹⁹, M. Vrsatil²⁶, M. L. Vázquez Acosta⁷⁵, S. J. Wagner¹¹⁰, R. Wagner^{115,137}, S. P. Wakely⁶⁰, R. Walter¹²⁵, J. E. Ward²⁵, J. J. Watson⁴⁷, A. Weinstein¹³⁸, M. White¹²⁹, R. White¹⁸, A. Wiercholska¹⁰⁰, P. Wilcox⁹⁴, D. A. Williams¹³⁹, R. Wischnewski⁷⁶, P. Wojcik⁷⁹, T. Yamamoto⁸⁹, H. Yamamoto⁷³, R. Yamazaki¹¹⁸, S. Yanagita⁹⁵, L. Yang⁹⁹, T. Yoshida⁹⁵, M. Yoshida⁸⁸, S. Yoshiike⁷³, T. Yoshikoshi⁹, M. Zacharias¹¹⁰, L. Zampieri³⁵, R. Zanin⁸⁰, M. Zavrtanik⁹⁹, D. Zavrtanik⁹⁹, A. Zdziarski¹⁰⁹, A. Zech⁴, H. Zechlin⁵⁸, V. Zhdanov⁶⁶, A. Ziegler⁶⁴, and J. Zorn⁷⁶

¹ CEA/IRFU/Sap, CEA Saclay, Bat 709, Orme des Merisiers, F-91191 Gif-sur-Yvette, France² Osservatorio Astrofisico di Arcetri, Largo E. Fermi, 5, I-50125 Firenze, Italy³ INFN Dipartimento di Scienze Fisiche e Chimiche—Università degli Studi dell’Aquila and Gran Sasso Science Institute, Via Vetoio 1, Viale Crispi 7, I-67100 L’Aquila, Italy⁴ LUTH and GEPI, Observatoire de Paris, CNRS, PSL Research University, 5 place Jules Janssen, F-92190, Meudon, France⁵ INAF—Osservatorio Astronomico di Roma, Via di Frascati 33, I-00040, Monteporzio Catone, Italy⁶ INFN Sezione di Napoli, Via Cintia, ed. G, I-80126 Napoli, Italy⁷ Department of Physics and Centre for Advanced Instrumentation, Durham University, South Road, Durham DH1 3LE, UK

- ⁸ Grupo de Altas Energías, Universidad Complutense de Madrid., Av Complutense s/n, E-28040 Madrid, Spain
- ⁹ Institute for Cosmic Ray Research, University of Tokyo, 5-1-5, Kashi-wanoha, Kashiwa, Chiba 277-8582, Japan
- ¹⁰ School of Physics, University of New South Wales, Sydney NSW 2052, Australia
- ¹¹ University of Namibia, Department of Physics, 340 Mandume Ndemufayo Ave., Pioneerspark Windhoek, Namibia
- ¹² School of Physics and Astronomy, Monash University, Melbourne, Victoria 3800, Australia
- ¹³ Astronomical Institute Anton Pannekoek, University of Amsterdam, Science Park 904 1098 XH Amsterdam, The Netherlands
- ¹⁴ Department of Physics, Graduate School of Science, University of Tokyo, 7-3-1 Hongo, Bunkyo-ku, Tokyo 113-0033, Japan
- ¹⁵ Research Center for the Early Universe, School of Science, University of Tokyo, 7-3-1 Hongo, Bunkyo-ku, Tokyo 113-0033, Japan
- ¹⁶ Riken, Institute of Physical and Chemical Research, 2-1 Hirosawa, Wako, Saitama, 351-0198, Japan
- ¹⁷ Harvard-Smithsonian Center for Astrophysics, 60 Garden St., Cambridge, MA 02180, USA
- ¹⁸ Max-Planck-Institut für Kernphysik, Saupfercheckweg 1, D-69117 Heidelberg, Germany
- ¹⁹ Institute for Applied Problems in Mechanics and Mathematics, 3B Naukova Street, Lviv, 79060, Ukraine
- ²⁰ INFN—Osservatorio Astrofisico di Torino, Italy, Corso Fiume 4, I-10133 Torino, Italy
- ²¹ ETH Zurich, Institute for Particle Physics, Schafmattstr. 20, CH-8093 Zurich, Switzerland
- ²² Astronomical Observatory of Ivan Franko National University of Lviv, 1 Universytetska Street, City of Lviv, 79000, Ukraine
- ²³ Politecnico di Bari and INFN Bari, Italy
- ²⁴ Université Paris-Sud, Institut de Physique Nucléaire d'Orsay (IPNO, IN2P3/CNRS et Université Paris-Sud, UMR 8608), 15 rue Georges Clemenceau, F-91406 Orsay, Cedex, France
- ²⁵ Institut de Física d'Altes Energies (IFAE), The Barcelona Institute of Science and Technology, Campus UAB, E-08193 Bellaterra (Barcelona), Spain
- ²⁶ Institute of Physics of the Academy of Sciences of the Czech Republic, Na Slovance 1999/2, 182 21 Praha 8, Czech Republic
- ²⁷ INFN—Osservatorio Astrofisico di Catania, Via S. Sofia, 78, I-95123 Catania, Italy
- ²⁸ Radboud University Nijmegen, P.O. Box 9010, 6500 GL Nijmegen, The Netherlands
- ²⁹ INFN—Osservatorio Astronomico di Brera, Via Brera 28, I-20121 Milano, Italy
- ³⁰ Institut de Recherche en Astrophysique et Planétologie, IRAP, 9 avenue Colonel Roche, BP 44346, F-31028 Toulouse Cedex 4, France
- ³¹ Laboratoire Univers et Particules de Montpellier, Université de Montpellier, CNRS/IN2P3, CC 72, Place Eugène Bataillon, F-34095 Montpellier Cedex 5, France
- ³² Department of Physics, Washington University, St. Louis, MO 63130, USA
- ³³ Istituto di Astrofisica Spaziale e Fisica Cosmica- Bologna, Via Piero Gobetti 101, I-40129 Bologna, Italy
- ³⁴ Faculty of Physics, University of Warsaw, ul. Hoża 69, 00-681 Warsaw, Poland
- ³⁵ INFN—Osservatorio Astronomico di Padova, Vicolo dell'Osservatorio 5, I-35122 Padova, Italy
- ³⁶ Dipartimento di Fisica—Università degli Studi di Padova, Via Marzolo 8, I-35131 Padova, Italy
- ³⁷ Centre for Space Research, North-West University, Potchefstroom Campus, 2531, South Africa
- ³⁸ Kavli Institute for Particle Astrophysics and Cosmology, Department of Physics and SLAC National Accelerator Laboratory, Stanford University, 2575 Sand Hill Road, Menlo Park, CA 94025, USA
- ³⁹ INFN—Istituto di Astrofisica Spaziale e Fisica Cosmica di Palermo, Via U. La Malfa 153, I-90146 Palermo, Italy
- ⁴⁰ Universidade Cruzeiro do Sul, Núcleo de Astrofísica Teórica (NAT/UCS), Rua Galvão Bueno 8687, Bloco B, sala 16, Liberdade 01506-000—São Paulo, Brazil
- ⁴¹ Istituto di Astrofisica Spaziale e Fisica Cosmica, Via Bassini 15, I-20133 Milano, Italy
- ⁴² INFN Sezione di Pisa, Largo Pontecorvo 3, I-56217 Pisa, Italy
- ⁴³ University of the Witwatersrand, 1 Jan Smuts Avenue, Braamfontein, 2000 Johannesburg, South Africa
- ⁴⁴ Pontificia Universidad Católica de Chile, Avda. Libertador Bernardo O' Higgins No 340, borough and city of Santiago, Chile
- ⁴⁵ Dublin City University, Glasnevin, Dublin 9, Ireland
- ⁴⁶ Department of Physics, Kindai University, Kowakae, Higashi-Osaka 577-8502, Japan
- ⁴⁷ University of Oxford, Department of Physics, 1 Keble Road, Oxford OX1 3NP, UK
- ⁴⁸ Istituto di Radioastronomia, INFN, INFN-IRA, Via Gobetti 101, Bologna, Italy
- ⁴⁹ INFN Sezione di Perugia, Via A. Pascoli, I-06123 Perugia, Italy
- ⁵⁰ Cherenkov Telescope Array Observatory, Saupfercheckweg 1, D-69117 Heidelberg, Germany
- ⁵¹ Instituto de Astronomia, Geofísica, e Ciências Atmosféricas, Universidade de São Paulo, Cidade Universitária, R. do Matão, 1226, CEP 05508-090, São Paulo, SP, Brazil
- ⁵² University of Udine & INFN Sezione di Trieste, Via delle Scienze 208, I-33100 Udine, Italy
- ⁵³ Laboratoire Leprince-Ringuet, École Polytechnique (UMR 7638, CNRS), F-91128 Palaiseau, France
- ⁵⁴ INFN Sezione di Bari, via Orabona 4, I-70126 Bari, Italy
- ⁵⁵ CIEMAT, Avda. Complutense 40, E-28040 Madrid, Spain
- ⁵⁶ University of Geneva—Département de physique nucléaire et corpusculaire, 24 rue du Général-Dufour, 1211 Genève 4, Switzerland
- ⁵⁷ INFN Sezione di Roma Tor Vergata, Via della Ricerca Scientifica 1, I-00133 Rome, Italy
- ⁵⁸ INFN Sezione di Torino, Via P. Giuria 1, I-10125 Torino, Italy
- ⁵⁹ University of Bari and INFN Bari, Italy
- ⁶⁰ Enrico Fermi Institute, University of Chicago, 5640 South Ellis Avenue, Chicago, IL 60637, USA
- ⁶¹ Institut für Physik & Astronomie, Universität Potsdam, Karl-Liebknecht-Strasse 24/25, D-14476 Potsdam, Germany
- ⁶² Department of Physics, TU Dortmund University, Otto-Hahn-Str. 4, D-44221 Dortmund, Germany
- ⁶³ Institute for Theoretical Physics and Astrophysics, Universität Würzburg, Campus Hubland Nord, Emil-Fischer-Str. 31, D-97074 Würzburg, Germany
- ⁶⁴ Universität Erlangen-Nürnberg, Physikalisches Institut, Erwin-Rommel-Str. 1, D-91058 Erlangen, Germany
- ⁶⁵ Escola de Artes, Ciências e Humanidades, Universidade de São Paulo, Rua Arlindo Bettio, 1000 São Paulo, CEP 03828-000, Brazil
- ⁶⁶ Astronomical Observatory of Taras Shevchenko National University of Kyiv, 60 Volodymyrska Street, City of Kyiv, 01033, Ukraine
- ⁶⁷ CEA/IRFU/SEDI, CEA Saclay, Bat 141, F-91191 Gif-sur-Yvette, France
- ⁶⁸ Laboratoire d'Annecy-le-Vieux de Physique des Particules, Université de Savoie, CNRS/IN2P3, 9 Chemin de Bellevue—BP 110, F-74941 Annecy-le-Vieux Cedex, France
- ⁶⁹ Western Sydney University, Locked Bag 1797, Penrith, NSW 2751, Australia
- ⁷⁰ Unitat de Física de les Radiacions, Departament de Física, and CERES-IEEC, Universitat Autònoma de Barcelona, E-08193 Bellaterra, Spain, Edifici Cc, Campus UAB, E-08193 Bellaterra, Spain
- ⁷¹ Grupo de Electronica, Universidad Complutense de Madrid, Av. Complutense s/n, E-28040 Madrid, Spain
- ⁷² Department of Earth and Space Science, Graduate School of Science, Osaka University, Toyonaka 560-0043, Japan
- ⁷³ Department of Physics and Astrophysics, Nagoya University, Chikusa-ku, Nagoya, 464-8602, Japan; sano@phys.nagoya-u.ac.jp
- ⁷⁴ Physik-Institut, Universität Zürich, Winterthurerstrasse 190, 8057 Zürich, Switzerland
- ⁷⁵ Instituto de Astrofísica de Canarias, Via Lactea, E-38205 La Laguna, Tenerife, Spain
- ⁷⁶ Deutsches Elektronen-Synchrotron, Platanenallee 6, D-15738 Zeuthen, Germany
- ⁷⁷ CEA/IRFU/SPP, CEA-Saclay, Bât 141, F-91191 Gif-sur-Yvette, France

- ⁷⁸ APC, Univ Paris Diderot, CNRS/IN2P3, CEA/Irfu, Obs de Paris, Sorbonne Paris Cité, France, 10, rue Alice Domon et Léonie Duquet, 75205 Paris Cedex 13, France
- ⁷⁹ Academic Computer Centre CYFRONET AGH, ul. Nawojki 11, 30-950 Cracow, Poland
- ⁸⁰ Departament de Física Quàntica i Astrofísica, Institut de Ciències del Cosmos, Universitat de Barcelona, IEEC-UB, Martí i Franquès, 1, E-08028, Barcelona, Spain
- ⁸¹ Department of Natural Sciences, The Open University of Israel, 1 University Road, POB 808, Raanana 43537, Israel
- ⁸² Sydney Institute for Astronomy, School of Physics, The University of Sydney, NSW 2006, Australia
- ⁸³ Department of Physics, Yamagata University, Yamagata, Yamagata 990-8560, Japan; nakamori@sci.kj.yamagata-u.ac.jp
- ⁸⁴ Universidad Técnica Federico Santa María, Avenida España 1680, Valparaíso, Chile
- ⁸⁵ Faculty of Management Information, Yamanashi-Gakuin University, Kofu, Yamanashi 400-8575, Japan
- ⁸⁶ Department of Physics, Columbia University, 538 West 120th Street, New York, NY 10027, USA
- ⁸⁷ The University of Manitoba, 540 Machray Hall, Winnipeg, Manitoba R3T 2N2, Canada
- ⁸⁸ Department of Physics, Tokai University, 4-1-1, Kita-Kaname, Hiratsuka, Kanagawa 259-1292, Japan
- ⁸⁹ Department of Physics, Konan University, Kobe, Hyogo, 658-8501, Japan
- ⁹⁰ Division of Theoretical Astronomy, National Astronomical Observatory of Japan, Osawa 2-21-1, Mitaka, Tokyo 181-8588, Japan
- ⁹¹ Institute of Space and Astronautical Sciences, Japan Aerospace Exploration Agency, 3-1-1 Yoshinodai, Chuo-ku, Sagami-hara, Kanagawa 252-5210, Japan
- ⁹² Yukawa Institute for Theoretical Physics, Kyoto University, Kyoto 606-8502, Japan
- ⁹³ INFN Sezione di Roma La Sapienza, P.le Aldo Moro, 2, I-00185 Roma, Italy
- ⁹⁴ University of Iowa, Department of Physics and Astronomy, Van Allen Hall, Iowa City, IA 52242, USA
- ⁹⁵ Faculty of Science, Ibaraki University, Mito, Ibaraki, 310-8512, Japan; hideaki.katagiri.sci@vc.ibaraki.ac.jp
- ⁹⁶ Universidad Católica del Norte, Av. Angamos 0610, Antofagasta, Chile
- ⁹⁷ Institute of Particle and Nuclear Studies, KEK (High Energy Accelerator Research Organization), 1-1 Oho, Tsukuba, 305-0801, Japan
- ⁹⁸ Division of Physics and Astronomy, Graduate School of Science, Kyoto University, Sakyo-ku, Kyoto, 606-8502, Japan
- ⁹⁹ Laboratory for Astroparticle Physics, University of Nova Gorica, Vipavska 13, 5000 Nova Gorica, Slovenia
- ¹⁰⁰ The Henryk Niewodniczański Institute of Nuclear Physics, Polish Academy of Sciences, ul. Radzikowskiego 152, 31-342 Cracow, Poland
- ¹⁰¹ Department of Physics and Astronomy, University of Leicester, Leicester, LE1 7RH, UK
- ¹⁰² Sorbonne Universités, UPMC, Université Paris Diderot, Sorbonne Paris Cité, CNRS, Laboratoire de Physique Nucléaire et de Hautes Energies (LPNHE), 4 Place Jussieu, F-75252, Paris Cedex 5, France
- ¹⁰³ Tuorla Observatory, University of Turku, FI-21500 Piikkiö, Finland
- ¹⁰⁴ Department of Physics, Humboldt University Berlin, Newtonstr. 15, D-12489 Berlin, Germany
- ¹⁰⁵ University of Trieste & INFN Sezione di Trieste, Italy
- ¹⁰⁶ Escuela Politécnica Superior de Jaén, Universidad de Jaén, Campus Las Lagunillas s/n, Edif. A3, E-23071 Jaén, Spain
- ¹⁰⁷ Institute for Nuclear Research and Nuclear Energy, BAS, 72 boul. Tsarigradsko chaussee, 1784 Sofia, Bulgaria
- ¹⁰⁸ Hiroshima Astrophysical Science Center, Hiroshima University, Higashi-Hiroshima, Hiroshima 739-8526, Japan
- ¹⁰⁹ Copernicus Astronomical Center, Polish Academy of Sciences, ul. Bartycka 18, 00-716 Warsaw, Poland
- ¹¹⁰ Landessternwarte, Universität Heidelberg, Königstuhl, D-69117 Heidelberg, Germany
- ¹¹¹ Department of Applied Physics, University of Miyazaki, 1-1 Gakuen Kibana-dai Nishi, Miyazaki, 889-2192, Japan
- ¹¹² University of Bath, Claverton Down, Bath BA2 7AY, UK
- ¹¹³ School of Allied Health Sciences, Kitasato University, Sagami-hara, Kanagawa 228-8555, Japan
- ¹¹⁴ Graduate School of Science and Engineering, Saitama University, 255 Simo-Ohkubo, Sakura-ku, Saitama city, Saitama 338-8570, Japan
- ¹¹⁵ Max-Planck-Institut für Physik, Föhringer Ring 6, D-80805 München, Germany
- ¹¹⁶ University of Białystok, Faculty of Physics, ul. K. Ciołkowskiego 1L, 15-254 Białystok, Poland
- ¹¹⁷ Charles University, Institute of Particle & Nuclear Physics, V Holešovičkách 2, 180 00 Prague 8, Czech Republic
- ¹¹⁸ Department of Physics and Mathematics, Aoyama Gakuin University, Fuchinobe, Sagami-hara, Kanagawa, 229-8558, Japan
ryo@phys.aoyama.ac.jp, ohira@phys.aoyama.ac.jp
- ¹¹⁹ Institute for Space-Earth Environmental Research, Nagoya University, Chikusa-ku, Nagoya 464-8601, Japan
- ¹²⁰ Department of Physics and Astronomy, University of California, Los Angeles, CA 90095, USA
- ¹²¹ Graduate School of Science and Technology, Tokushima University, Tokushima 770-8506, Japan
- ¹²² Faculty of Physics, Astronomy and Applied Computer Science, Jagiellonian University, ul. prof. Stanisława Łojasiewicza 11, 30-348 Kraków, Poland
- ¹²³ Osservatorio Astronomico di Trieste and INFN Sezione di Trieste, Via delle Scienze 208 I-33100 Udine, Italy
- ¹²⁴ Institut de Planétologie et d'Astrophysique de Grenoble, INSU/CNRS, Université Joseph Fourier, 621 Avenue centrale, Domaine Universitaire, F-38041 Grenoble Cedex 9, France
- ¹²⁵ ISDC Data Centre for Astrophysics, Observatory of Geneva, University of Geneva, Chemin d'Ecogia 16, CH-1290 Versoix, Switzerland
- ¹²⁶ University College Dublin, Belfield, Dublin 4, Ireland
- ¹²⁷ Institut für Astronomie und Astrophysik, Universität Tübingen, Sand 1, D-72076 Tübingen, Germany
- ¹²⁸ Institut für Astro- und Teilchenphysik, Leopold-Franzens-Universität, Technikerstr. 25/8, A-6020 Innsbruck, Austria
- ¹²⁹ School of Physical Sciences, University of Adelaide, Adelaide SA 5005, Australia
- ¹³⁰ Centro Brasileiro de Pesquisas Físicas, Rua Xavier Sigaud 150, RJ 22290-180, Rio de Janeiro, Brazil
- ¹³¹ Faculty of Physics and Applied Computer Science, University of Łódź, ul. Pomorska 149-153, 90-236 Łódź, Poland
- ¹³² Linnaeus University, Universitetsplatsen 1, SE-352 52 Växjö, Sweden
- ¹³³ Institute of Space Sciences (IEEC-CSIC) and Institució Catalana de Recerca i Estudis Avançats (ICREA), Campus UAB, Carrer de Can Magrans, s/n E-08193 Cerdanyola del Vallés, Spain
- ¹³⁴ Centre de Physique des Particules de Marseille (CPPM), Aix-Marseille Université, CNRS/IN2P3, Marseille, 163 Avenue de Luminy, F-13288 Marseille, France
- ¹³⁵ University of Wisconsin, Madison, 500 Lincoln Drive, Madison, WI, 53706, USA
- ¹³⁶ Instituto de Física de São Carlos, Universidade de São Paulo, Av. Trabalhador São-carlense, 400—CEP 13566-590, São Carlos, SP, Brazil
- ¹³⁷ Stockholm University, Universitetsvägen 10 A, SE-10691 Stockholm, Sweden
- ¹³⁸ Department of Physics and Astronomy, Iowa State University, Zaffarano Hall, Ames, IA 50011-3160, USA
- ¹³⁹ Santa Cruz Institute for Particle Physics and Department of Physics, University of California, Santa Cruz, 1156 High Street, Santa Cruz, CA 95064, USA

Received 2016 July 14; revised 2017 April 10; accepted 2017 April 12; published 2017 May 9

Abstract

We perform simulations for future Cherenkov Telescope Array (CTA) observations of RX J1713.7–3946, a young supernova remnant (SNR) and one of the brightest sources ever discovered in very high energy (VHE) gamma rays. Special attention is paid to exploring possible spatial (anti)correlations of gamma rays with emission at other wavelengths, in particular X-rays and CO/HI emission. We present a series of simulated images of RX J1713.7

–3946 for CTA based on a set of observationally motivated models for the gamma-ray emission. In these models, VHE gamma rays produced by high-energy electrons are assumed to trace the nonthermal X-ray emission observed by *XMM-Newton*, whereas those originating from relativistic protons delineate the local gas distributions. The local atomic and molecular gas distributions are deduced by the NANTEN team from CO and HI observations. Our primary goal is to show how one can distinguish the emission mechanism(s) of the gamma rays (i.e., hadronic versus leptonic, or a mixture of the two) through information provided by their spatial distribution, spectra, and time variation. This work is the first attempt to quantitatively evaluate the capabilities of CTA to achieve various proposed scientific goals by observing this important cosmic particle accelerator.

Key words: cosmic rays – gamma rays: ISM – ISM: individual objects (RX J1713.7–3946, G347.3–0.5)

1. Introduction

1.1. Origin of Galactic Cosmic Rays

The origin of Galactic cosmic rays (CRs), protons with energies up to $10^{15.5}$ eV (the so-called “knee”), has been one of the long-standing problems in astrophysics (e.g., Blasi 2012; Drury 2012; Amato 2014). At present, young supernova remnants (SNRs) are the most probable candidates for being the major accelerators of CRs, which are sometimes also thought to have been potential “PeVatrons” (i.e., accelerators capable of producing charged particles at PeV scale). CRs of heavier species like iron may reach energies near the “second knee” at around 10^{17} eV. The detections of synchrotron X-rays in some SNRs have already shown evidence for the acceleration of electrons to ultrarelativistic energies at SNR shocks (Koyama et al. 1995). On the other hand, there remains the unresolved issue as to how efficiently SNRs are accelerating high-energy protons compared to electrons.

So far, VHE gamma-ray observations have revealed the existence of high-energy particles at the shock of young SNRs (e.g., Enomoto et al. 2002; Aharonian et al. 2004, 2005, 2006, 2007a, 2007b, 2009; Katagiri et al. 2005; Albert et al. 2007; Acero et al. 2010; Abramowski et al. 2011; Acciari et al. 2011; see also Ferrand & Safi-Harb 2012). Although the gamma rays are suggested to originate from either leptonic (low-energy photons upscattered by high-energy electrons) or hadronic (π^0 -decay photons generated by accelerated protons colliding with surrounding gas) processes, it is generally a nontrivial task to distinguish these processes despite abundant multiwavelength studies. As a result, we cannot yet provide an unequivocal proof for the paradigm that Galactic CRs are predominantly produced by young SNRs. It has been shown that the gamma-ray spectra of the middle-aged SNRs IC 443 and W44 have a sharp cutoff at low energies (~ 100 MeV), reminiscent of the π^0 bump that provides a direct proof for a hadronic origin of the gamma rays (Giuliani et al. 2011; Ackermann et al. 2013). However, the maximum CR energies inferred from the gamma rays detected in these SNRs are much lower than the “knee,” and their gamma-ray fluxes at VHE energies are very low (see, e.g., Uchiyama et al. 2010; Lee et al. 2015, for detailed emission models). We hence expect that the younger SNR population is more qualified to be PeVatron candidates.

The acceleration mechanisms of CRs have also been studied for a long time. As of today, the most plausible physical process is suggested to be the diffusive shock acceleration (DSA) mechanism (Blandford & Eichler 1987). This is supported by the observational fact that some young SNRs are found to be gamma-ray bright around their shock fronts. Recent development of the DSA theory has revealed that the back-reaction of the accelerated CRs, that is, their pressure

against the incoming super-Alfvén gas flow in the shock frame, cannot be neglected if a large number of nuclear particles are accelerated to relativistic energies (e.g., Drury 1983; Berezhko & Ellison 1999; Malkov & Drury 2001). This can lead to strong modifications of the shock structure and a nonlinear coupling between the shock flow and CR acceleration. Some observational results are consistent with the predictions of such nonlinear DSA (NLDSA) models (Bamba et al. 2003, 2005a; 2005b, Vink & Laming 2003; Warren et al. 2005; Uchiyama et al. 2007; Helder et al. 2009). However, whether these models can fully explain all aspects revealed by the accumulating multiwavelength observations still remains in doubt. For example, NLDSA models often predict a “concave” curvature in the CR spectrum in which the photon index decreases as CR energy increases. In such a case, the spectral index, s , of the accelerated particles around the shock can be harder than 2.0 near the maximum energy if the acceleration is highly efficient¹⁴⁰ (Malkov 1997; Berezhko & Ellison 1999; Kang et al. 2001). This prediction appears to contradict the CR spectral indices of $s \approx 2.2$ – 2.4 inferred from recent gamma-ray observations, radio spectral indices, and the CR spectrum at Earth. Recent modifications of the NLDSA theory did manage to reproduce indices softer than $s = 2.0$ by, for example, invoking feedback effects from the self-generated magnetic turbulence in the shock precursor (e.g., Caprioli et al. 2009; Ferrand et al. 2014b). Shock obliqueness and momentum dependence of the diffusion coefficient might be important for producing a softer index (e.g., Ferrand et al. 2014a). Another possible scenario is to consider the presence of neutral hydrogen in the acceleration region (Ohira et al. 2009; Blasi et al. 2012; Ohira 2012; Morlino et al. 2013). But the story is obviously far from complete before we reach an entire understanding of the plasma physics around strong collisionless shocks.

Furthermore, the important process of CR escape into the interstellar medium (ISM) is also uncertain. In general, the gamma-ray spectrum of young SNRs starts to decline around 10 TeV, so that the maximum energy of CRs is around 30–100 TeV. This is approximately two orders of magnitude lower than the knee energy. Therefore, to explain the knee feature in the CR spectrum at Earth, very young SNRs of ages $\lesssim 100$ yr are anticipated to experience a “PeVatron phase” (Gabici & Aharonian 2007), during which the highest-energy CRs are generated under strong magnetic fields associated with high-velocity shocks (Völk et al. 2005) and released into the ISM. However, we do not yet understand in detail when and how these high-energy particles escape from their acceleration sites to become Galactic CRs.

¹⁴⁰ We consider a CR energy spectrum in the form of $dN(E)/dE \propto E^{-s}$, where E is the CR energy.

1.2. Origin of Gamma Rays from SNR RX J1713.7–3946

RX J1713.7–3946 (also known as a radio SNR G347.3–0.5; Slane et al. 1999), one of the brightest VHE gamma-ray sources ever detected (Muraishi et al. 2000; Enomoto et al. 2002; Aharonian et al. 2004, 2006, 2007a), is an ideal target to study these unresolved mysteries. The distance and age of RX J1713.7–3946 are estimated to be 0.9–1.3 kpc and ~ 1600 yr, respectively (Fukui et al. 2003; Moriguchi et al. 2005), which is consistent with its connection with the guest star AD393 (e.g., Wang et al. 1997). This age estimate is supported by its fast shock velocity (Katsuda et al. 2015) and the similarities of its other observed properties to other young SNRs. So far, in comparison with other young shell-type SNRs, the VHE gamma-ray spectrum of RX J1713.7–3946 is the most precisely measured over a wide energy band (from 0.3 to 100 TeV) thanks to its high brightness. In addition to VHE gamma rays, observations in other wavebands are also available. These include lower-energy gamma rays detected by the *Fermi* Large Area Telescope (*Fermi*/LAT), synchrotron radio emission and X-rays, and radio line emission from CO molecules and HI gas. Although weak thermal X-ray emission has recently been detected from the SNR interior (Katsuda et al. 2015), the X-ray emission is still dominated by synchrotron radiation, which links directly to the existence of high-energy electrons. Radio observations of CO and HI gas have revealed a highly inhomogeneous medium surrounding the SNR, such as clumpy molecular clouds (Fukui et al. 2003, 2012; Fukui 2013; Moriguchi et al. 2005; Sano et al. 2010, 2013, 2015). Another radio observation of CS also confirmed the existence of a very dense ($>10^5 \text{ cm}^{-3}$) ISM core toward the SNR (Maxted et al. 2012). We are also aware that some of these characteristics are common among several other young SNRs, including RX J0852.0–4622 (Aharonian et al. 2005, 2007b; Katagiri et al. 2005), RCW 86 (Aharonian et al. 2009), and HESS J1731–347 (Abramowski et al. 2011). It is noteworthy that no thermal X-ray emission has been firmly detected in these SNRs (e.g., Koyama et al. 1997; Tsunemi et al. 2000; Bamba et al. 2012).

Prior to the *Fermi* era, the VHE gamma-ray spectrum of RX J1713.7–3946 above 300 GeV measured by H.E.S.S. was often suggested to be best explained by a hadronic model (Aharonian et al. 2006, 2007a) in which the gamma rays originate from the decay of π^0 mesons produced by CR protons interacting with the local gas. However, as *Fermi*/LAT measured the gamma-ray spectrum of RX J1713.7–3946 in the 3–300 GeV energy range, it turned out that the photon index (1.5 ± 0.1) is one more typically expected from leptonic (i.e., inverse Compton) emission from high-energy electrons with a spectral index of $s = 2.0$ (Abdo et al. 2011). *Fermi* also reported a smooth connection between the hard GeV spectrum and the TeV domain with a spectral index of 2.02 ± 0.23 for $E > 50$ GeV up to 1 TeV (Ackermann et al. 2016). The conclusion on the leptonic origin of the gamma rays from this remnant has been reached by recent theoretical modelings (e.g., Ellison et al. 2010; Lee et al. 2012). In this case, the flux ratio between synchrotron X-rays and inverse Compton gamma rays suggests a magnetic field strength of $B \sim 10\text{--}20 \mu\text{G}$. At first sight, this kind of value is inconsistent with the simple interpretation for the observed time variability (Uchiyama et al. 2007) and thin filamentary structures (Bamba et al. 2005b; Parizot et al. 2006) of synchrotron X-rays through a fast energy loss of high-energy electrons, which typically requires

$B \gtrsim 100 \mu\text{G}$. Recent X-ray observations of the SNR RX J0852.0–4622, which show very similar features to RX J1713.7–3946, have however recovered a shallow steepening of the synchrotron index behind the shock as a function of radius, suggesting an average magnetic field near the shock of only a few μG (Kishishita et al. 2013). This has been shown to be consistent with theoretical models (Lee et al. 2013). It has also been proposed that a fast X-ray time variability does not necessarily require high magnetic fields in extended regions behind the shock. For example, Bykov (2008) has shown that a steeply falling electron distribution in a turbulent magnetic field can produce intermittent synchrotron emission consistent with the observations. The thin filament of synchrotron X-rays might be explained if the downstream magnetohydrodynamic turbulence damps exponentially (Pohl et al. 2005), although a critical assessment has been given for the case of RX J1713.7–3946 (Marcowith & Casse 2010). It is worth noticing that in the framework of a one-zone leptonic model the IC emission on cosmic microwave background photons only cannot explain the observed gamma-ray flux, which, on the contrary, requires a high level of IR background radiation about 20 times larger than the Galactic average at the position of RX J1713.7–3946 (see Morlino et al. (2009)). These seemingly contradictory observational facts and competing interpretations have led to much uncertainty in the quest to unravel the true origin of the gamma-ray emission from nonthermal SNRs like RX J1713.7–3946. This age-old issue awaits a final resolution by the utilization of observatories with higher performance in the near future.

Alternatively, there are possibilities that a hadronic model for the gamma-ray emission of RX J1713.7–3946 remains viable despite its hard spectrum. For example, in extreme cases, NLDSA models can produce a proton index of 1.5 (Yamazaki et al. 2009), resulting in a hard slope of the hadronic gamma rays consistent with the *Fermi* observation. Another plausible scenario can be pictured by considering the effect of shock–cloud interaction, which is strongly suggested by recent results of CO and HI observations toward RX J1713.7–3946 (Fukui et al. 2012). The higher the energy of the CR protons is, the deeper they can penetrate into the central (i.e., high-density) part of the dense cloud cores inside a highly inhomogeneous gas environment. Depending on the total mass fraction and the energy dependence of the CR penetration depth in such dense cores in a clumpy medium interacting with the shock, an overall hard gamma-ray spectrum consistent with the *Fermi*/LAT and H.E.S.S. data can be realized (Zirakashvili & Aharonian 2010; Inoue et al. 2012; Gabici & Aharonian 2014). On the other hand, it has been argued that since a hadronic model requires a high ambient gas density in order for the gamma-ray emission to be dominated by the π^0 -decay component, bright thermal X-ray emission should be expected from the shocked gas, which is nevertheless not detected so far (e.g., Ellison et al. 2012). In a shock–cloud interaction scenario, however, it is quite possible that the dense clumps of gas swept up by the blast wave can remain “intact” and stay at a low average ionization state and temperature. If these dense clumps bear a significant mass fraction behind the shock, faint thermal X-rays can be naturally explained (Inoue et al. 2012).

Furthermore, a strong magnetic field ($B \sim 0.1\text{--}1$ mG) can be automatically generated by the turbulent dynamo downstream of the shock that is interacting with a clumpy medium, even without considering the amplification of turbulent magnetic

field driven by the streaming CR protons in the shock precursor. A potential difficulty one can face is that if $B \sim \text{mG}$ and the gamma-ray emission is mostly hadronic, to explain the measured flux of radio synchrotron emitted by electrons, the primary electron-to-proton ratio at the SNR should be anomalously small, i.e., $K_{ep} \sim 10^{-6}$ (Uchiyama et al. 2003; Butt 2008). This is far below the observed value at Earth and the typical estimated values in the nearby galaxies (Katz & Waxman 2008). This might be resolved if the electrons are accelerated in the later stages of SNR evolution relative to the protons so that K_{ep} can be different from the present value (Tanaka et al. 2008), although this is still highly speculative and further discussions are necessary.

Another possibility that may offer an explanation to the gamma-ray spectrum is that the gamma rays are contributed by a roughly comparable mixture of leptonic and hadronic components. However, this scenario seems unlikely because of the apparently energy-independent gamma-ray morphology (Aharonian et al. 2006). The smooth, single-peak spectral shape without any features would require fine-tuning of model parameters describing the two populations. We should also note that the accurate determination of the mix of leptonic and hadronic components is made difficult by the H.E.S.S. point-spread function (PSF).

Our best hope to make progress on our understanding of this very important CR accelerator relies on better data from powerful future telescopes. The Cherenkov Telescope Array (CTA) is a next-generation observatory of imaging air Cherenkov telescopes (IACTs), which consists of an array of large-, medium-, and small-sized IACTs distributed over a 1 km^2 area (Actis et al. 2011; Acharya et al. 2013). The CTA will achieve better angular resolution and higher sensitivity in a wider energy range than the current IACT generation (see the following section). It is expected that we can obtain the most stringent constraints on theoretical models through their comparison with CTA data on RX J1713.7–3946 and multi-wavelength observations of this intriguing object.

In this paper, we study prospects for CTA observations of RX J1713.7–3946. In Section 2, we summarize the scientific objectives related to the capabilities of CTA. In Section 3, we describe in depth our simulation models and the results. Discussions and summary can be found in Section 4.

2. Linking CTA Capabilities with Key Scientific Goals

The identification of the emission mechanism of gamma rays from nonthermal SNRs like RX J1713.7–3946 is of utmost importance for advancing cosmic-ray physics. We will evaluate the capabilities of CTA on serving this purpose as follows. First, we perform morphological studies in order to assess the possibility of using spatial information to pin down the major component of the VHE gamma-ray emission from leptonic and hadronic origins. In the case where the leptonic component is dominant, we can proceed to check the capability of CTA to search for a possible “additional” hadronic component using spectral analyses. We will also evaluate the prospect of detecting a time variation of the spectral cutoff energy over a relatively long timescale, which we believe is a very useful and unique approach for identifying the VHE emission mechanism.

1. *Imaging with good spatial resolution.* CTA is designed to reach angular resolutions of arcminute scale at TeV energies, which is at least a factor of three better than H.

E.S.S. (Actis et al. 2011). This improvement is critical in our present study because the resolution of CTA will catch up with that of current CO and HI gas observations in the radio waveband and also get closer to that of X-ray images such as those obtained by *XMM-Newton*. Synchrotron X-rays are enhanced around the CO and HI clumps on a length scale of a few parsecs,¹⁴¹ but are relatively faint inside the clumps on a subparsec scale. In other words, the peaks in X-ray brightness are offset from those of the CO/HI gas distribution (Sano et al. 2013). Indeed, there exist many gas clumps whose associated X-ray peaks are located more than 0.05 deg away from their centers. If the gamma rays are leptonic in origin and if the energy spectra of the CR protons are spatially uniform, we expect that the gamma rays possess brightness peaks coincident with the CO/HI gas clumps and show similar spatial offsets to the X-rays.

2. *Broadband gamma-ray spectrum.* CTA will cover photon energies from 20 GeV to 100 TeV with a sensitivity about 10 times better than H.E.S.S. (Actis et al. 2011). The spectrum of RX J1713.7–3946 measured by H.E.S.S. is well described by a single smooth component. However, it is possible that there exists another dimmer, and harder, component at the high-energy end of the spectrum that H.E.S.S. cannot discern owing to its insufficient effective area. More specifically, if the gamma-ray spectrum is described by an inverse Compton component with a primary electron index $s = 2.0$, which has been inferred from the *Fermi*/LAT observation (Abdo et al. 2011), there can exist an accompanying hadronic component from the CR protons with the same spectral index. This hadronic component should appear flat in νF_ν space, and its expected flux is

$$\nu F_\nu \approx 3 \times 10^{-12} \text{ erg cm}^{-2} \text{ s}^{-1} \times \left(\frac{E_{\text{CR}}}{3 \times 10^{49} \text{ erg}} \right) \left(\frac{n}{1 \text{ cm}^{-3}} \right), \quad (1)$$

where we have assumed the distance to RX J1713.7–3946 to be 1 kpc. The quantities E_{CR} and n are the total CR proton energy in the emission sites and the average target gas density, respectively. By adopting the values $E_{\text{CR}} = 3 \times 10^{49} \text{ erg}$ and $n = 1 \text{ cm}^{-3}$ as in Equation (1), this flux is about 10% of the currently observed νF_ν spectral peak at a photon energy of $\sim \text{TeV}$; such a hard component can dominate at the high-energy end of the gamma-ray spectrum and will be discernible as a spectral hardening feature by CTA.

Note that a dim hadronic component can be dominant at the highest gamma-ray energies only if the maximum energy E_{max} of the parent CR proton spectrum is not lower than $\sim 100 \text{ TeV}$, and that such a high value of E_{max} is not guaranteed. In particular, if we assume the simplest one-zone model with the DSA around the shock of RX J1713.7–3946, as well as an inverse Compton origin for the gamma rays, then the maximum electron energy, $\sim 70 \text{ TeV}$, is not limited by energy loss but by the SNR age or CR escape to far upstream because of the weak average magnetic field strength of $\sim 10 \mu\text{G}$ required for a leptonic scenario, so that the maximum proton energy is basically similar to that of electrons. However,

¹⁴¹ $1 \text{ pc} \approx 0.06 \text{ deg}$ at a distance of 1 kpc.

the emergence of a dim hadronic emission component with a maximum energy of more than 50 TeV is still possible if we consider a multizone model. Multizone models may be motivated by the observational results discussed in Section 1.2, which seem to be inconsistent with each other.¹⁴² For example, a small amount of protons, which were accelerated when the SNR was younger and the magnetic field was stronger, could have escaped the acceleration region and are hitting the surrounding molecular clouds now to produce dim hadronic gamma-ray emission, while most of the gamma rays are produced by either electrons or protons that are currently being accelerated. Assuming a Bohm-like diffusion in magnetic turbulence with an average strength of ~ 0.1 mG, the propagation length of PeV protons within 10^3 yr is estimated to be ~ 1 pc, so that a non-negligible fraction of such high-energy protons can exist inside and around the SNR to interact with dense targets. Spatially resolved spectroscopy with the better angular resolution of CTA will help us investigate such “multizone” structures. Another possible scenario is the following. Both protons and electrons are currently being accelerated, but protons are accelerated in regions with stronger magnetic fields, while electrons are accelerated in regions with weaker magnetic fields. In the strong magnetic field regions, electrons are less efficiently accelerated, because the Alfvén Mach number is small owing to the strong upstream magnetic field, resulting in a small injection rate of electrons (Hoshino & Shimada 2002). Generally speaking, if a young SNR is producing CRs up to the knee energy, we naturally expect a dim hadronic component with gamma-ray energy more than 100 TeV unless the hadrons have escaped into the ISM during an earlier phase. Note that this statement is independent from the detailed acceleration mechanism. Therefore, if such a dim and hard hadronic component were detected, it would provide evidence for proton acceleration up to the knee energy.

3. *Time variation of maximum CR energies.* The CTA observatory will last for more than 10 yr. This motivates us to measure any possible time variation of the gamma-ray spectrum over long timescales. It has been shown that the maximum energy of CRs confined in SNRs depends on the SNR age during the Sedov phase (e.g., Ptuskin & Zirakashvili 2003; Ohira et al. 2012). Since the downstream magnetic field strength around the shock decays with the shock velocity, as the SNR ages it becomes harder to confine high-energy CRs through pitch-angle scatterings near the shock. Accordingly, the maximum energy of CR protons should also decrease with time.¹⁴³

The overall normalization of the gamma-ray spectrum may also change with time, although its behavior is

highly uncertain. Assuming that the energy in cosmic-ray protons is proportional to the integration of the kinetic energy flux of upstream matter passing through the shock front, Dwarkadas (2013) derived a simple scaling of hadronic gamma-ray luminosity, which can be written as $L_\gamma \propto t^{5m-2m\beta-2}$, where the SNR radius evolves as $R \propto t^m$ and the surrounding medium has a power-law profile in density $\rho \propto r^{-\beta}$. Then, for a uniform surrounding medium ($\beta = 0$), we obtain $L_\gamma \propto t^3$ for $m = 1$ (free expansion) and $L_\gamma \propto t^0$ for $m = 2/5$ (adiabatic expansion). In the case of $\beta = 2$ (an isotropic wind), we find $L_\gamma \propto t^{-1}$ for $m = 1$ (free expansion) and $L_\gamma \propto t^{-4/3}$ for $m = 2/3$ (adiabatic expansion). Another model predicts a secular flux increase at a few hundred GeV at a level around 15% over 10 yr (Federici et al. 2015).

In the following, we consider the simplest case in which only the cutoff energy of the gamma-ray spectrum changes with time. The cutoff energy may vary $\sim 10\%$ in 10–20 yr. To demonstrate this, we consider a power-law behavior for the time evolution of the escape-limited maximum energy, i.e., $E_{\max,p} \propto t^{-\alpha}$. The value of α is important for understanding the average source spectrum of Galactic CRs, which should be steeper than E^{-2} (Ohira et al. 2010). Although there are theoretical studies on α (e.g., Ptuskin & Zirakashvili 2003; Yan et al. 2012), its precise value has not yet been determined observationally or theoretically. To reproduce the spectrum of Galactic CRs, we can phenomenologically assume that $E_{\max,p} \approx 10^{15.5}$ eV at the beginning of the Sedov phase (t_{Sedov}), and that $E_{\max,p} \approx 1$ GeV at the end of the Sedov phase ($\approx 10^{2.5} t_{\text{Sedov}}$), from which we can obtain $\alpha \approx 2.6$ (Ohira et al. 2010). The age of RX J1713.7–3946 is around 10^3 yr (Section 1.2). Then, the expected evolution rate of the maximum energy at this age is estimated as $\dot{E}_{\max,p}/E_{\max,p} \approx -\alpha/t \approx -2.6 \times 10^{-3} \text{ yr}^{-1}$. This implies a decay of the maximum energy of about 5% over a period of 20 yr. If the observed gamma rays are produced by CR protons, the cutoff energy of the gamma rays is proportional to $E_{\max,p}$. On the other hand, the leptonic gamma-ray scenario predicts the cutoff energy to be proportional to $E_{\max,e}^2$. Therefore, the time variation of the cutoff energy of gamma rays over 20 yr is expected to be about 5% and 10% for CR protons and electrons, respectively. These estimations are based on the assumption of a smooth transition of $E_{\max,p}$ or $E_{\max,e}$ with a power-law scaling. However, RX J1713.7–3946 is thought to be currently interacting with dense regions. If so, a collision between the SNR shock and density bumps causes a sudden deceleration of the shock, which results in a variability of $E_{\max,p}$ and/or $E_{\max,e}$ on shorter timescales.

For the CR electrons, if their maximum energy, $E_{\max,e}$, is also limited by their escape from the SNR, its time evolution should be the same as that of the CR protons. On the other hand, if it is limited by synchrotron cooling, its evolution should differ from that of the CR protons. A cooling-limited $E_{\max,e}$ near the shock can either decrease or increase with time depending on the evolution of the amplified magnetic field (Ohira et al. 2012), for which shock–cloud interactions can play a significant role.

¹⁴² For instance, if the gamma-ray emission is leptonic, the magnetic field is weaker than those suggested by rapid variability and thin filaments of synchrotron X-rays (if their origins are associated with fast electron cooling near the cutoff, which may or may not be the case). Another example is that the number density of the local gas should be small to explain the nondetection of thermal X-ray lines. This situation may be unlikely if we take into account the fact that this SNR is apparently interacting with dense molecular clouds, although it depends much on the timing of the shock–cloud interaction.

¹⁴³ In the Sedov phase, the maximum energy of CR protons should no longer be constrained by the acceleration timescale, but rather by the CR escape process.

3. Simulations

In this section, we evaluate the feasibility of achieving the scientific objectives discussed above using a series of observation simulations for CTA. The simulation software package *ctools*¹⁴⁴ (Knödolseder et al. 2013, 2016) that we use in this study is developed as an open source project aiming at a versatile analysis tool for the broader gamma-ray astronomy community, and it is very similar to the *Science Tools*¹⁴⁵ developed for the *Fermi*/LAT data analysis. *ctobssim* is an observation simulator that generates event files containing the reconstructed incident photon direction in sky coordinates, reconstructed energy, and arrival time for each VHE photon detected in the field of view. Simulated VHE sky images are produced by *ctskymap* using the simulated event files. Event selection based on these parameters can be applied by *ctselect*, and event binning is performed by *ctbin*. Unbinned or binned likelihood model fitting is executed through *ctlike*.

3.1. Input Data

3.1.1. Instrumental Information and Backgrounds

To conduct CTA simulations and analyses, we used a set of instrument response functions (IRFs) equivalent to those for the public “2Q” array configuration available at the CTA Web site.¹⁴⁶ 50 hr point-source observations at a zenith angle of 20° are assumed to generate the IRFs. We assumed here observations pointing toward the center of the remnant.

We modeled the spatial distribution of the isotropic background, which originates from gamma-like charged cosmic-ray events, as a two-dimensional Gaussian in the field of view (due to the radial dependence of acceptance) with a standard deviation σ of 3° throughout these studies. Since RX J1713.7–3946 is located on the Galactic plane, we also took into account the Galactic diffuse background (GDBG). We conservatively assumed that the GDBG has a power-law spectrum without a cutoff and estimated it by extrapolating the GDBD model *gll_iem_v05_rev1.fit*¹⁴⁷ provided by the *Fermi*/LAT team (Acero et al. 2016). Using only six data points above 0.1 TeV in the *Fermi*/LAT data up to >513 GeV, we derived a net GDBG flux within 1 degree around RX J1713.7–3946 of $1.04 \times 10^{-9} (E/0.1 \text{ TeV})^{-2.24}$ photons $\text{cm}^{-2} \text{ s}^{-1} \text{ TeV}^{-1}$, which is also roughly consistent with previous TeV observations (Abramowski et al. 2014). With these assumptions, the GDBG exceeds the isotropic cosmic-ray background above a few TeV.

3.1.2. Gamma Rays from RX J1713.7–3946

Here we assume that the gamma-ray spectrum is dominated by a leptonic component. As discussed in the previous section, an additional hadronic component should exist. By combining these two components, we made templates for our gamma-ray simulations as follows:

1. *Leptonic component.* We used the X-ray image of RX J1713.7–3946 as a template that traces the leptonic gamma-ray morphology. The X-ray image is extracted

from the *XMM-Newton* archival data consisting of multiple pointing observations to cover the entirety of this remnant. The energy band of this image is restricted to 0.5–8.0 keV. The non-X-ray background is subtracted, and vignetting and exposure corrections are applied. The pixel scale is 5″, and the image is smoothed with a Gaussian function with a σ of 3 pixels. Apparent point sources, likely foreground stars or background extragalactic objects, as well as the central compact object (CCO) known as the neutron star candidate 1WGA J1713.4–3949 (Lazendic et al. 2003), the brightest point source in this field, are excluded.

We consider a simplified case where the gamma-ray spectral shape is spatially invariant over the two-dimensional image. The spectrum we adopt is based on the fitting results from H.E.S.S. data and can be written as

$$\frac{dN_e}{dE}(E) = A_e \times \left(\frac{E}{\text{TeV}}\right)^{-\Gamma_e} \exp(-E/E_c^e), \quad (2)$$

where A_e is a normalization constant, Γ_e is the photon index (2.04), and E_c^e is the cutoff energy (17.9 TeV) (see Table 4 of Aharonian et al. 2007a).

2. *Hadronic component.* Based on CO and HI observations, we obtain the total target gas column density (atomic + molecular; Fukui et al. 2012) and use it as a template that is assumed to trace the hadronic gamma-ray morphology. The spatial boundary of the total target gas is defined using the apparent edge of the VHE gamma-ray emission shown in Aharonian et al. (2007a). Additionally, we assumed that the spatial distribution of CR protons is homogeneous within the shell of the SNR. Again, the gamma-ray spectral shape is assumed to be spatially invariant. In this case the spectrum is written in a parametric form, i.e.,

$$\frac{dN_p}{dE}(E) = A_p \times \left(\frac{E}{\text{TeV}}\right)^{-\Gamma_p} \exp(-E/E_c^p), \quad (3)$$

where A_p , Γ_p , and E_c^p are the normalization constant, photon index, and cutoff energy, respectively.

We adopt $\Gamma_p = 2.0$ and $E_c^p = 300$ TeV as our fiducial parameters to picture a possible PeVatron accelerator. In the following, we consider several cases with different values of A_p/A_e . The absolute values of A_e and A_p are determined by requiring that the integration of the sum $N_e(E) + N_p(E)$ is equal to the total photon flux between 1 and 10 TeV measured by H. E.S.S.

We generated gamma rays with energies between 0.3 and 100 TeV, which is narrower than the designed energy range of CTA in full-array configurations. Since the spectral shape is concave below a few hundred GeV (Abdo et al. 2011), we restricted the simulation and analysis to above 0.3 TeV for simplicity. On the other hand, setting a high enough upper energy bound is extremely important with the aforementioned scientific goals in mind. Unfortunately, however, the IRF currently available supports simulations only up to $10^{2.2} \sim 158$ TeV, so that we simply cut our event generations at 100 TeV in this pilot simulation study. In the near future the IRF will be updated and the energy coverage will be extended to 300 TeV and beyond. Working with such IRFs and more detailed emission models are reserved for future work.

¹⁴⁴ Version 00-07-01. See also <http://ascl.net/1601.005> (ascl.1601.005).

¹⁴⁵ <http://fermi.gsfc.nasa.gov/ssc/data/analysis/software/>

¹⁴⁶ <https://portal.cta-observatory.org/Pages/CTA-Performance.aspx> (version 2015-05-05).

¹⁴⁷ Available at <http://fermi.gsfc.nasa.gov/ssc/data/access/lat/BackgroundModels.html>.

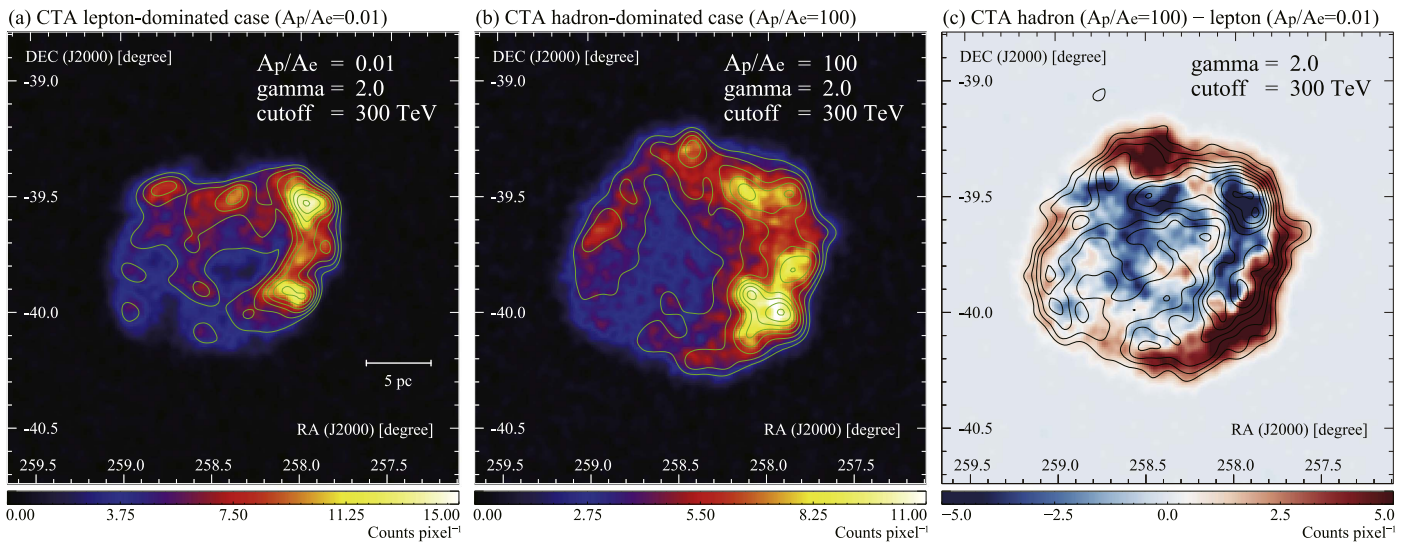


Figure 1. Simulated gamma-ray images of (a) $A_p/A_e = 0.01$ (lepton-dominated case) and (b) $A_p/A_e = 100$ (hadron-dominated case) with $\Gamma_p = 2.0$ and $E_p^c = 300$ TeV. The green contours show (a) *XMM-Newton* X-ray intensity (e.g., Acero et al. 2009) and (b) total interstellar proton column density (Fukui et al. 2012) smoothed to match the PSF of CTA. The subtracted image of (b) – (a) is also shown in (c). The black contours correspond to the H.E.S.S. VHE gamma rays (Aharonian et al. 2007a). The unit of color axis is counts pixel⁻¹ for all panels.

3.2. Results and Analysis

3.2.1. Gamma-ray Image

We first look at the simulated images for CTA and study the possibility of using morphological information to determine the major component of the VHE gamma-ray emission. Different gamma-ray images in the energy range of 1–100 TeV are generated by changing A_p/A_e , the ratio between the hadronic and leptonic contributions. Figures 1(a) and (b) show the images for $A_p/A_e = 0.01$ (lepton dominated; e.g., Abdo et al. 2011) and 100 (hadron dominated; e.g., Fukui et al. 2012), respectively. Each image corresponds to 50 hr of observations with CTA. As per our assumptions described above for the underlying templates, the lepton-dominated model (Figure 1(a)) shows a gamma-ray image that resembles the X-rays, and the hadron-dominated case (Figure 1(b)) delineates the ISM proton distribution including both CO and H I. The difference between them (Figure 1(c)) is significant, as is evident from the subtraction between the two images.

To perform a quantitative evaluation, we employ the method of likelihood fitting (e.g., Mattox et al. 1996; Cowan 1998; Feigelson & Babu 2012). We focus here on the ability of CTA to determine the dominant emission component from the prospectively observed morphology. We calculated the maximum log-likelihood, L_e and L_p , by fitting the simulated images with the leptonic and hadronic spatial template, respectively. We note that the templates used during the fits are the same as those used in the simulations, meaning that a rather idealistic case is assumed. To determine the log-likelihoods L_e and L_p individually, we employ either the hadronic or leptonic template one at a time in each fitting model (regardless of the intrinsic A_p/A_e ratio in the simulation data being fitted). We keep the normalization, photon index, and cutoff energy of the power law as free parameters during the fitting process. We also fit the data with the composite model containing both the leptonic and hadronic components in order to obtain the log-likelihood L_{ep} . Then we calculated the differences $2(L_{ep} - L_e)$ and $2(L_{ep} - L_p)$ for various A_p/A_e , as summarized in Table 1. These differences in log-

Table 1
Differences in the Maximum Log-likelihood for Spatial Templates with Various Values of the A_p/A_e Ratio

A_p/A_e^a	$2(L_{ep} - L_e)^b$	$2(L_{ep} - L_p)^b$
0.01	16.8	20085.8
0.1	761.9	15030.1
1.0	12280.2	3494.1
10.0	27083.1	171.9
100	31649.0	0.9

Notes.

^a A_e and A_p are normalization constants for the leptonic and hadronic component, respectively. The details are described in the text.

^b L_e , L_p , and L_{ep} are the maximum log-likelihoods for the leptonic, hadronic, and composite templates, respectively.

likelihood are large when the composite model is a significant improvement over the leptonic or hadronic models, and the difference is intended to be distributed approximately as a χ^2 variable with 3 degrees of freedom (for the extra parameters in the composite model). However, this is only a rough indication, as the conditions of Wilks’s theorem are violated because the simple model is on the physical boundary of allowed parameters of the composite model (Wilks 1938). Table 1 indicates that the composite model is strongly favored over the simple models and that we can easily find the dominant component when the contribution of the second component is small. For example, when $A_p/A_e = 100$, L_{ep} is very different from L_e but nearly the same as L_p . On the other hand, in the case where there is a more or less equal contribution from both particle populations (i.e., $A_p/A_e = 1$), we found that the fitting tends to be biased toward the hadronic component. When $A_p/A_e = 1$ in our model, the total number of hadronic photons is larger than that of the leptonic photons owing to the differences in E_c , especially at higher energies. Since the angular resolution becomes better at such higher energy ranges, the likelihood result expectedly favors a hadron-dominated scenario. Nevertheless, we note that the case of $A_p/A_e > 1$ (hadron dominated) shows a more spread-

Table 2Resulting Parameters of the Likelihood Analyses for the Simulation Data with Various Values of the A_p/A_e Ratio

A_p/A_e^a	$2(L_{ep} - L_e)^b$	Γ_e^c	E_c^{cd}	Γ_p^e
0.01	9.2	2.03 ± 0.01	17.08 ± 0.56	1.73 ± 0.26
0.02	41.9	2.03 ± 0.01	17.50 ± 0.60	1.86 ± 0.12
0.06	346.5	2.04 ± 0.01	17.62 ± 0.66	1.90 ± 0.04
0.10	998.0	2.03 ± 0.01	17.00 ± 0.67	1.93 ± 0.03

Notes.^a A_e and A_p are normalization constants for the leptonic and hadronic component, respectively. The details are described in the text.^b L and L_0 are the maximum log-likelihoods for the model with/without the hadronic component, respectively.^c Γ_e is a photon index for the gamma-ray spectrum of the leptonic component.^d E_c is a cutoff energy for the gamma-ray spectrum of the leptonic component.^e Γ_p is a photon index for the gamma-ray spectrum of the hadronic component.

out structure in gamma rays than that of $A_p/A_e < 1$ (lepton dominated). This trend is consistent with the latest H.E.S.S. results (Abdalla et al. 2016). We conclude that CTA observations will be able to distinguish between hadronic and leptonic gamma rays based on morphological characterizations.

3.2.2. Spectrum

In the case where the leptonic component is dominant, we can subsequently attempt to search for the “hidden” hard component with a hadronic origin as discussed above. In order to evaluate the capability of CTA to achieve this interesting task, we further perform likelihood analyses over the wider energy band of $E > 0.3$ TeV using 50 hr of simulation data with various assumed A_p/A_e ratios. The spatial templates and the spectral shapes in the fitting models are the same as those used originally for the simulation. The fitting results are summarized in Table 2. We can significantly detect the hadronic component even for a small $A_p/A_e = 0.02$. However, the best-fit spectral shape for the hadronic component is generally slightly harder than the true input value of 2.0 for the cases with smaller ratios. This is probably because the dimmer and widely extended hadronic component is more easily confused with the background photons, especially at lower energies. Indeed, when we simulated and analyzed without the GDBG or the cosmic-ray background, the best-fit photon indices were converged consistent with the input value of 2.0. We thus refrain from drawing any strong conclusion on the detectability of the A_p/A_e ratio at this point.

We proceed to perform maximum likelihood fits for the simulation data (with a ratio $A_p/A_e = 0.1$) for 18 logarithmically spaced energy bands spanning from 0.3 to 100 TeV. Unlike our analysis above, where we have to specify spectral shapes for the hadronic and leptonic components, in this way we can measure the spectrum independently of any spectral model assumption. Figure 2 shows the resulting spectrum from our “bin-by-bin” analysis of the same 50 hr simulation data. For each spatial template, it is clear that our likelihood fits satisfactorily reproduce the simulated spectrum above 0.3 TeV. The data in each energy bin were fit by power laws with a fixed index of 2.0. As a final check, we compared the total gamma-ray flux points from the likelihood fit over the 18 energy bins with our simulation model in which the emission is purely leptonic (see Figure 3). Although it depends on the energy

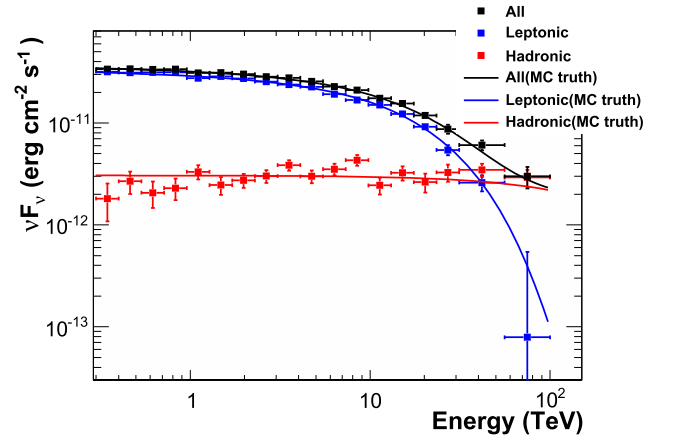


Figure 2. Spectral energy distribution of the gamma-ray emission obtained by analyzing the CTA simulation data for RX J1713.7–3946. The blue and red squares are the spectral points for the leptonic and hadronic spatial templates, respectively. Vertical bars show statistical errors. The black squares are the total fluxes of the leptonic and hadronic components. The black vertical bars are the errors for the total fluxes obtained by adding the errors for two components in quadrature. The blue, red, and black solid lines show the input spectra for the leptonic component, the hadronic component, and the total, respectively.

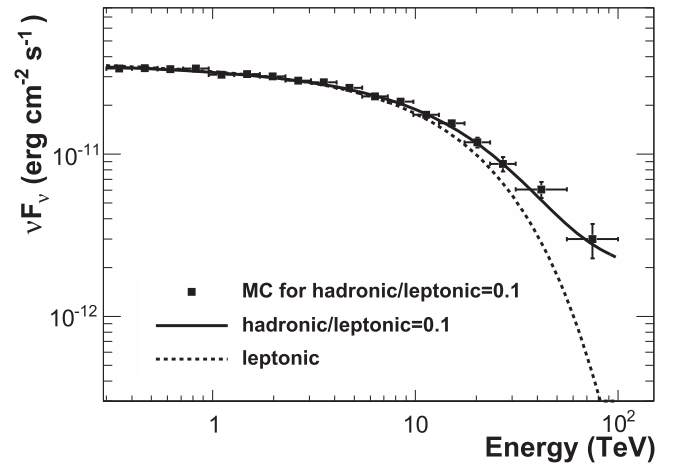


Figure 3. Comparison of the spectral energy distribution of the gamma-ray emission obtained by analyzing the CTA simulation data for RX J1713.7–3946 with the models. The black squares are the total of the fluxes for the leptonic and hadronic spatial templates. Horizontal bars indicate the energy range the flux refers to. Vertical bars show the errors obtained by adding the errors for two components in quadrature. The solid line shows the input spectra of gamma-ray simulation. The dotted line is for the model when the emission is purely leptonic.

binning, in the case of $A_p/A_e = 0.1$ and 50 hr of observation, we can obtain the flux points above 30 TeV deviating from the purely leptonic model with a statistical significance level of $>3\sigma$. Thus, we reach the conclusion that 50 hr of CTA observation could detect at above 3σ the hard hadronic component with a ratio $A_p/A_e = 0.1$, under the idealistic conditions assumed here.

3.2.3. Time Variation of Cutoff Energy

Detecting the time variation of the cutoff energy of the gamma-ray spectrum provides a clue to distinguish between different emission scenarios and CR acceleration theories. We start off with the generation of simulated photons for a 100 hr observation of RX J1713.7–3946. The simulations are

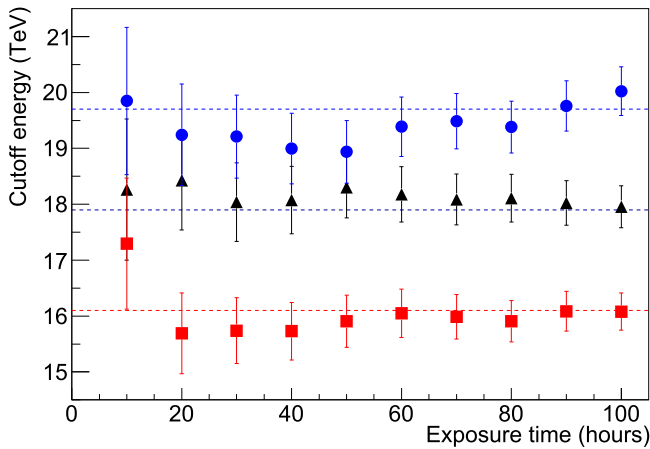


Figure 4. Best-fit cutoff energies derived from our spectral analyses as a function of observation time. Circles, triangles, and squares correspond to the case of $\Delta E_c/E_c = +10\%$, 0% , and -10% , respectively. Dashed lines indicate the true values of the simulations.

performed for three sets of intrinsic cutoff energies at 17.9, 19.7, and 16.1 TeV each. The first set with $E_c = 17.9$ TeV is tagged as our nominal case based on the current best-fit value suggested by H.E.S.S. data. The other two cases represent the possibility of a varying E_c in the coming years within the CTA mission lifetime. As a start, we consider a variation of $\Delta E_c/E_c = \pm 10\%$ to obtain an initial impression on how sensitive CTA will be to such fractional changes in the spectral cutoff. Roughly ~ 10 yr could be expected for $\pm 10\%$ variation, as discussed in Section 2. Here we consider the purely leptonic scenario as an example (see Section 3.1 for details).

For each case, we explore how the detectability depends on the total exposure time by extracting subsets from the full data set with different exposures shorter than 100 hr. This is achieved by applying a time-based cut using *ctselect*. We then perform unbinned likelihood fitting for each of these subsets to derive the corresponding best-fit cutoff energies. In the fitting, the normalization, photon index, and E_c^e are all free parameters and are fitted simultaneously. Figure 4 shows the best-fit E_c^e and their associated errors from our likelihood analyses. As expected, the fitted E_c^e are closer to their true values, with smaller uncertainties for longer exposures in all cases.

We then proceed to define a significance, s , for any observed E_c^e variation as

$$s_{\pm}(t) = \frac{|E_{\pm}(t) - E_0(t)|}{\sqrt{\sigma_{\pm}^2(t) + \sigma_0^2(t)}}, \quad (4)$$

where E_0 and E_{\pm} are the best-fit E_c for the cases with the nominal value and $\pm 10\%$ variation, respectively. σ_0 and σ_{\pm} are the corresponding errors. To suppress statistical fluctuations, we repeat all of our simulations for 100 times and take the average of the calculated $s(t)$ from all runs. In the top left panel of Figure 5, our result indicates that a decrease in E_c with time is slightly easier to identify than an increase, which can be understood as follows. In the energy range of E_c (~ 10 TeV), the sensitivity of CTA begins to drop with energy. As a result, a lower cutoff energy can actually be measured more easily and precisely for a given exposure. Our result is hence consistent with expectations. We perform a simple fit to the points by a function $\propto \sqrt{t}$, where t is the exposure. If we observe > 70 hr in

the two epochs, we are able to achieve a 3σ detection for the $\Delta E_c/E_c = -10\%$ case, whereas ~ 100 hr are necessary for the $+10\%$ case.

We can also estimate $s(t)$ from another point of view by considering the following observation scenario. Supposing that we will observe RX J1713.7–3946 with different exposures during the first and second epochs, how does the detection significance of a variation in E_c depend on the observation time in each epoch? In this case, we can calculate

$$s_{\pm}(t_1, t_2) = \frac{|E_{\pm}(t_2) - E_0(t_1)|}{\sqrt{\sigma_{\pm}^2(t_2) + \sigma_0^2(t_1)}}, \quad (5)$$

where t_1 and t_2 are the exposure times for the first and second epoch, respectively. Our result is presented in the top right and bottom left panels of Figure 5. Here we again arrive at the conclusion that an increase of E_c is harder to detect. A longer exposure in the first year apparently makes it easier for us to detect the variation with a shorter observation in the next epoch. Although several combinations of observation time are available for the 3σ detection, 50 hr is the minimum required for the first observation period.

Since the full operation of CTA will begin roughly 10 yr after the H.E.S.S. observations, it is also of interest to know whether it is possible to detect any variation of E_c by comparing previous H.E.S.S. results and the upcoming CTA observations. In this context, we can calculate $s(t)$ again by Equation (4), fixing $E_0 = 17.9$ TeV and $\sigma_0 = 3.3$ TeV (Aharonian et al. 2007a), and repeat the same procedure described above. The result is plotted in Figure 5 (bottom right panel). Owing to the large uncertainty of the H.E.S.S. results, however, the expected significance remains low and unmeaningful even with long CTA exposures up to 100 hr. This result consolidates the necessity of performing CTA observations of RX J1713.7–3946 in at least two epochs separated by a ~ 10 yr time interval.

4. Summary and Discussion

In this paper, we have studied the feasibility and prospects for achieving a set of key scientific goals through CTA observations of RX J1713.7–3946, based on simulations with exposures of 50 hr or above. We showed that a 50 hr observation is adequate to identify the dominant gamma-ray emission component, namely, leptonic or hadronic, from the morphology of the SNR that is going to be revealed by CTA. And we should be able not only to quantify both the leptonic and hadronic components but also to detect a possible hidden hard component at $> 3\sigma$ level through spectral analyses if they are mixed with a ratio of $A_p/A_e \geq 0.1$. Interestingly, we also found that CTA will be able to reveal fractional variations of the spectral cutoff energy over a timescale of ~ 10 yr, for the very first time. A variation of $\Delta E_c/E_c = \pm 10\%$ is found to be detectable provided that an exposure time longer than 50 hr can be secured for the first epoch. The result may indicate that the detection would be a tough task, but at the same time the achievable science convinces us that it is worth the challenge.

The uncertainties of our results presented above are purely statistical. The energy dispersion and uncertainty in the measured energy scale can affect the fidelity of the spectral analyses especially in the measurement of E_c . We confirmed that the significance of the E_c variations due to the predicted energy dispersion would be negligible, while the expected

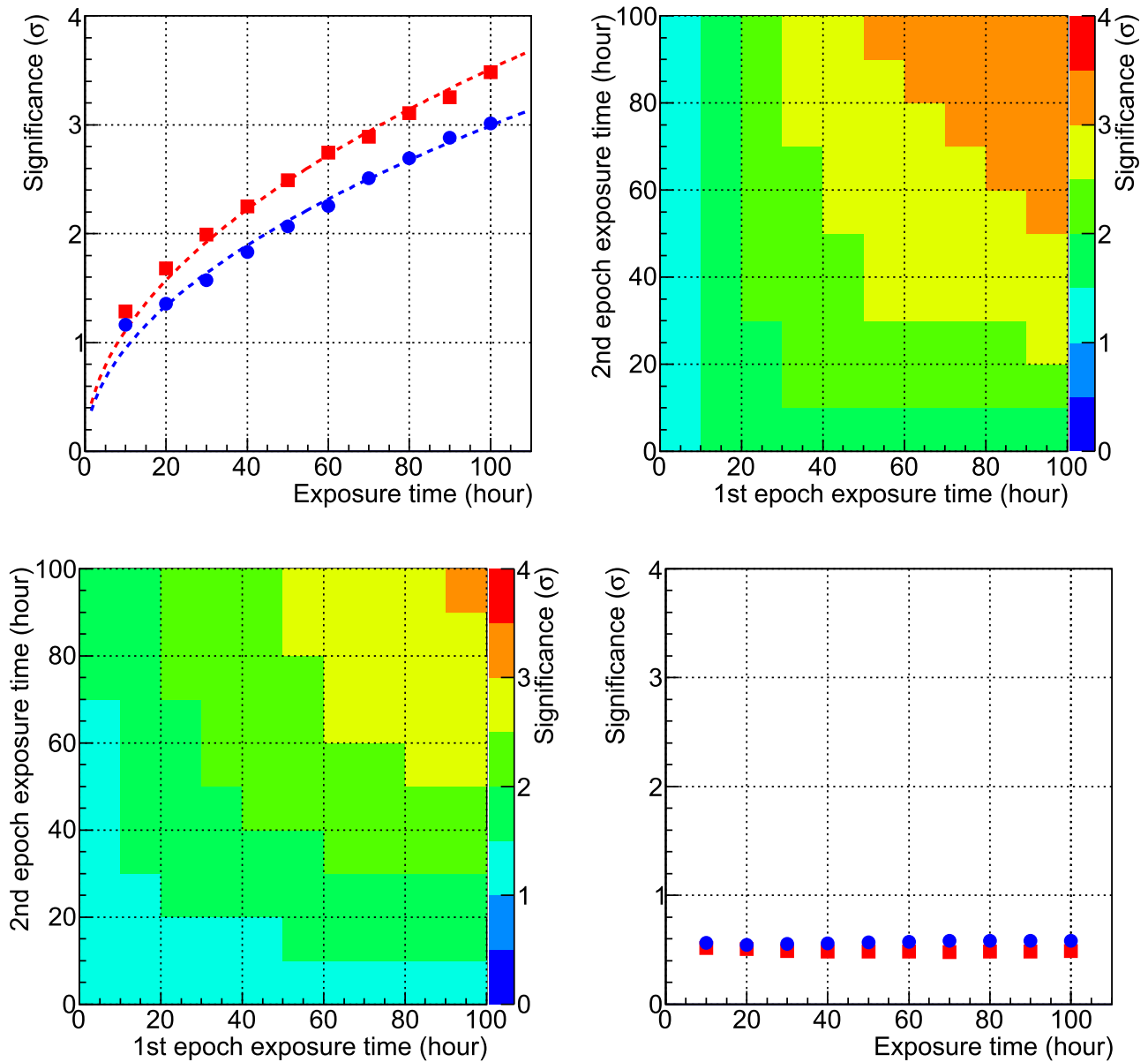


Figure 5. Significance of the detected variation of E_c as a function of exposure time for three observation scenarios (see text for detail). Top left panel: same exposure time for the two epochs of observations. Dashed lines represent the best-fit curve for each data set. Squares and circles represent results for the $\Delta E_c/E_c = -10\%$ and $+10\%$ case, respectively. Top right panel: results for various exposure times for the first and second data set for the $\Delta E_c/E_c = -10\%$ case. Bottom left panel: same as the top right panel, but for the $\Delta E_c/E_c = +10\%$ case. Bottom right panel: scenario of using H.E.S.S. results for the first epoch (Aharonian et al. 2007a). Squares and circles represent results for the $\Delta E_c/E_c = -10\%$ and $+10\%$ case, respectively.

energy scale uncertainty would cause $\sim \pm 1\sigma$ deviations, respectively. We also confirmed that the contamination of the very faint thermal X-ray to the leptonic template and variations of the hadronic template due to the uncertainty of the radio observations are both negligible to the results. Katsuda et al. (2015) reported the detection of very faint thermal components, but their spectral analysis region is limited only in the very center of this SNR, with a radius of 5/3. They also presented the softness map, and the analysis is performed on one of the softest regions where the thermal component is brighter than other areas. Even in such a region, the flux of the thermal emission is far less than 10% of the synchrotron. Concerning the radio map, the uncertainty of the intensity is estimated to be less than 10%. When we modified the hadronic image template by multiplying a random factor conservatively between $\pm 10\%$ to every image pixel, the

results are very similar and differences are typically less than 1σ . Estimating other systematic uncertainties for our analysis is not trivial and can be highly model dependent. Possible effects due to a deviation from the actual PSF profile with a tail¹⁴⁸ may exist, since the PSF was assumed simply as a Gaussian in our simulations. Since RX J1713.7–3946 is located at the Galactic plane, the source is expected to be contaminated by the Galactic diffuse gamma-ray emission, which constitutes the majority of the background events (i.e., “noise” for our purpose). The possible existence of currently unknown TeV sources nearby, such as the CCO 1WGA J1713.4–3939, for instance, can contribute to the systematic errors in such a crowded region on the Galactic plane.

¹⁴⁸ As presented and discussed in Aleksić et al. (2016) for the case of MAGIC telescopes.

On the other hand, CTA will measure gamma rays with energies far below 0.3 TeV, where the *Fermi*/LAT and H.E.S.S. data points connect. If the gamma rays are mostly of a leptonic origin and the magnetic field strength B is around 10 or a few tens of μG , which has been inferred from theoretical studies (e.g., Yamazaki et al. 2009; Ellison et al. 2010; Lee et al. 2012), we expect that the electron spectrum possesses a cooling break (Longair 1994) at $\approx 7.5 \text{ TeV } (B/40 \mu\text{G})^{-2} (t_{\text{age}}/10^3 \text{ yr})^{-1}$, where t_{age} is the age of RX J1713.7–3946. In this case the gamma-ray spectrum must also exhibit a corresponding break at $E_b \approx 0.3 \text{ TeV } (B/40 \mu\text{G})^{-4} (t_{\text{age}}/10^3 \text{ yr})^{-2}$ (since $E_\gamma \propto E_e^2$ for inverse Compton emission in the Thomson regime), if the particle injection is impulsive. Future identification of such a cooling break feature in the gamma-ray spectrum by CTA will equip us with a powerful and independent tool to measure the value of B , which would bring important constraints on the particle acceleration mechanism at high Mach number collisionless shocks.

Our present study is based on a fairly simplified input model, but can be extended to include more physics motivated by theoretical models. Some possibilities are listed in the following, and their incorporation in our model is reserved for future works.

- (1) *Hadronic model based on MHD simulations*: The shock interaction with dense clouds excites turbulence, which amplifies the magnetic field up to the mG order (Inoue et al. 2012; Sano et al. 2013, 2015). These results may be crucial for our better understanding of the gamma-ray and X-ray images of SNRs. Under these circumstances, the CR electrons will be significantly affected via synchrotron cooling for magnetic fields greater than 100 μG , and the gamma-ray image will follow if the leptonic gamma-ray production is important. In order to fully understand such effects on the gamma-ray images, we need to incorporate the shock–cloud interaction by utilizing the ISM distribution with a reasonably high angular resolution and detailed numerical simulations. Using the full performance of CTA by lowering the energy threshold could be essential in these studies, since more apparent differences between the leptonic and hadronic scenarios are expected.
- (2) *Highest-energy CRs from SNRs*: Accelerated particles eventually escape from the SNR forward shock to become Galactic CRs. According to recent studies, the highest-energy CRs start to escape from the SNR at the beginning of the Sedov phase (Ptuskin & Zirakashvili 2005; Ohira et al. 2010; Ohira 2012). The escaped CRs make a gamma-ray halo, which is more extended than the SNR shell (Gabici et al. 2009; Fujita et al. 2010; Ohira et al. 2011). Spectral measurements of gamma-ray halos will provide information on the highest-energy CRs accelerated in the SNR in the past. Observed profiles of the gamma-ray halo will also constrain the diffusion coefficient of CRs and density structure in the ambient medium (Fujita et al. 2011; Malkov et al. 2013).
- (3) *Hydrodynamical models and spectral modifications via nonlinear effects*: More sophisticated models taking into account NLDSA processes predict realistic CR proton electron spectra (e.g., Zirakashvili & Aharonian 2010; Lee et al. 2012), both trapped and escaped, with a full treatment of their time evolution and spatial distribution

in a hydrodynamic calculation for RX J1713.7–3946. The comparison of these models with CTA results will provide important new insights on the very complex NLDSA mechanism at young SNRs.

This research made use of *ctools*, a community-developed analysis package for Imaging Air Cherenkov Telescope data. *ctools* is based on GammaLib, a community-developed toolbox for the high-level analysis of astronomical gamma-ray data.

We gratefully acknowledge financial support from the following agencies and organizations: Ministerio de Ciencia, Tecnología e Innovación Productiva (MinCyT), Comisión Nacional de Energía Atómica (CNEA), Consejo Nacional de Investigaciones Científicas y Técnicas (CONICET), Argentina; State Committee of Science of Armenia, Armenia; Conselho Nacional de Desenvolvimento Científico e Tecnológico (CNPq), Fundação de Amparo à Pesquisa do Estado do Rio de Janeiro (FAPERJ), Fundação de Amparo à Pesquisa do Estado de São Paulo (FAPESP), Brasil; Croatian Science Foundation, Croatia; Ministry of Education, Youth and Sports, MEYS LE13012, LG14019, 7AMB14AR005, and the Czech Science Foundation grant 14-17501S, Czech Republic; Ministry of Higher Education and Research, CNRS-INSU and CNRS-IN2P3, CEA-Irfu, ANR, Regional Council Ile de France, Labex ENIGMASS, OSUG2020 and OCEVU, France; Max Planck Society, BMBF, DESY, Helmholtz Association, Germany; Department of Atomic Energy, Department of Science and Technology, India; Istituto Nazionale di Astrofisica (INAF), Istituto Nazionale di Fisica Nucleare (INFN), MIUR, Italy; ICRR, University of Tokyo, JSPS, Japan; Netherlands Research School for Astronomy (NOVA), Netherlands Organization for Scientific Research (NWO), Netherlands; The Bergen Research Foundation, Norway; Ministry of Science and Higher Education, the National Centre for Research and Development and the National Science Centre, Poland; Slovenian Research Agency, Slovenia; MINECO support through the National R + D + I, Subprograma Severo Ochoa, CDTI funding plans and the CPAN and MultiDark Consolider-Ingenio 2010 program, Spain; Swedish Research Council, Royal Swedish Academy of Sciences, Sweden; Swiss National Science Foundation (SNSF), Ernest Boninchi Foundation, Switzerland; Durham University, Leverhulme Trust, Liverpool University, University of Leicester, University of Oxford, Royal Society, Science and Technologies Facilities Council, UK; U.S. National Science Foundation, U.S. Department of Energy, Argonne National Laboratory, Barnard College, University of California, University of Chicago, Columbia University, Georgia Institute of Technology, Institute for Nuclear and Particle Astrophysics (INPAC-MRPI program), Iowa State University, Washington University McDonnell Center for the Space Sciences, USA.

The research leading to these results has received funding from the European Union’s Seventh Framework Programme (FP7/2007-2013) under grant agreement no. 262053.

We thank S. Katsuda for providing the original *XMM-Newton* image.

References

- Abdalla, H., et al. (H.E.S.S. Collaboration) 2016, *A&A*, in press (arXiv:1609.08671)
- Abdo, A. A., Ackermann, M., Ajello, M., et al. 2011, *ApJ*, 734, 28
- Abramowski, A., Acero, F., Aharonian, F., et al. 2011, *A&A*, 531, A81

- Abramowski, A., Aharonian, F., Ait Benkhali, F., et al. 2014, *PhRvD*, **90**, 122007
- Acciari, V. A., Aliu, E., Arlen, T., et al. 2011, *ApJL*, **730**, L20
- Acero, F., Ackermann, M., Ajello, M., et al. 2016, *ApJS*, **223**, 26
- Acero, F., Aharonian, F., Akhperjanian, A. G., et al. 2010, *A&A*, **516**, A62
- Acero, F., Ballet, J., Decourchelle, A., et al. 2009, *A&A*, **505**, 157
- Acharya, B. S., Actis, M., Aghajani, T., et al. 2013, *Aph*, **43**, 3
- Ackermann, M., Ajello, M., Allafort, A., et al. 2013, *Sci*, **339**, 807
- Ackermann, M., Ajello, M., Atwood, W. B., et al. 2012, *ApJ*, **750**, 3
- Ackermann, M., Ajello, M., Atwood, W. B., et al. 2016, *ApJS*, **222**, 5
- Actis, M., Agnetta, G., Aharonian, F., et al. 2011, *ExA*, **32**, 193
- Aharonian, F., Akhperjanian, A. G., Aye, K.-M., et al. 2004, *Natur*, **432**, 75
- Aharonian, F., Akhperjanian, A. G., Barres de Almeida, U., et al. 2009, *ApJ*, **692**, 1500
- Aharonian, F., Akhperjanian, A. G., Bazer-Bachi, A. R., et al. 2005, *A&A*, **437**, L7
- Aharonian, F., Akhperjanian, A. G., Bazer-Bachi, A. R., et al. 2006, *A&A*, **449**, 233
- Aharonian, F., Akhperjanian, A. G., Bazer-Bachi, A. R., et al. 2007a, *A&A*, **464**, 235
- Aharonian, F., Akhperjanian, A. G., Bazer-Bachi, A. R., et al. 2007b, *ApJ*, **661**, 236
- Albert, J., Aliu, E., Anderhub, H., et al. 2007, *A&A*, **474**, 937
- Aleksić, J., Ansoldi, S., Antonelli, L. A., et al. 2016, *Aph*, **72**, 76
- Amato, E. 2014, *IJMPD*, **23**, 1430013
- Bamba, A., Pühlhofer, G., Acero, F., et al. 2012, *ApJ*, **756**, 149
- Bamba, A., Yamazaki, R., & Hiraga, J. 2005a, *ApJ*, **632**, 294
- Bamba, A., Yamazaki, R., Ueno, M., & Koyama, K. 2003, *ApJ*, **589**, 827
- Bamba, A., Yamazaki, R., Yoshida, T., Terasawa, T., & Koyama, K. 2005b, *ApJ*, **621**, 793
- Berezko, E. G., & Ellison, D. C. 1999, *ApJ*, **526**, 385
- Blandford, R. D., & Eichler, D. 1987, *PhR*, **154**, 1
- Blasi, P. 2012, *A&ARv*, **21**, 70
- Blasi, P., Morlino, G., Bandiera, R., Amato, E., & Caprioli, D. 2012, *ApJ*, **755**, 121
- Butt, Y. 2008, *MNRAS*, **386**, L20
- Bykov, A. M. 2008, *ApJ*, **689**, 133
- Caprioli, D., Blasi, P., Amato, E., & Vietri, M. 2009, *MNRAS*, **395**, 895
- Cowan, G. 1998, *Statistical Data Analysis* (Oxford: Clarendon Press)
- Drury, L. O. 'C. 1983, *RPPH*, **46**, 973
- Drury, L. O. 'C. 2012, *Aph*, **39**, 52
- Dwarkadas, V. V. 2013, *MNRAS*, **434**, 3368
- Ellison, D. C., Patnaude, D. J., Slane, P., & Raymond, J. 2010, *ApJ*, **712**, 287
- Ellison, D. C., Slane, P., Patnaude, D. J., & Bykov, A. M. 2012, *ApJ*, **744**, 39
- Enomoto, R., Tanimori, T., Naito, T., et al. 2002, *Natur*, **416**, 823
- Federici, S., Pohl, M., Telezhinsky, I., Wilhelm, A., & Dwarkadas, V. V. 2015, *A&A*, **577**, A12
- Feigelson, E. D., & Babu, G. J. 2012, *Modern Statistical Methods for Astronomy* (Cambridge: Cambridge Univ. Press)
- Ferrand, G., Danos, R. J., Shalchi, A., et al. 2014a, *ApJ*, **792**, 133
- Ferrand, G., Decourchelle, A., & Safi-Harb, S. 2014b, *ApJ*, **789**, 49
- Ferrand, G., & Safi-Harb, S. 2012, *AdSpR*, **49**, 1313
- Fujita, Y., Ohira, Y., & Takahara, F. 2010, *ApJL*, **712**, L153
- Fujita, Y., Takahara, F., Ohira, Y., & Iwasaki, K. 2011, *MNRAS*, **415**, 3434
- Fukui, Y. 2013, *ASSP*, **34**, 249
- Fukui, Y., Sano, H., Sato, J., et al. 2012, *ApJ*, **746**, 82
- Fukui, Y., Tamura, Y., Yamamoto, K., et al. 2003, *PASJ*, **55**, L61
- Gabici, S., & Aharonian, F. A. 2007, *ApJ*, **665**, 131
- Gabici, S., & Aharonian, F. A. 2014, arXiv:1406.2322
- Gabici, S., Aharonian, F. A., & Casanova, S. 2009, *MNRAS*, **396**, 1629
- Giuliani, A., Cardillo, M., Tavani, M., et al. 2011, *ApJL*, **742**, L30
- Helder, E. A., Vink, J., Bassa, C. G., et al. 2009, *Sci*, **325**, 719
- Hoshino, M., & Shimada, N. 2002, *ApJ*, **572**, 880
- Inoue, T., Yamazaki, R., Inutsuka, S.-I., & Fukui, Y. 2012, *ApJ*, **744**, 71
- Kang, H., Jones, T. W., LeVeque, R. J., & Shyue, K. M. 2001, *ApJ*, **550**, 737
- Katagiri, H., Enomoto, R., Ksenofontov, L. T., et al. 2005, *ApJL*, **619**, L163
- Katsuda, S., Acero, F., Tominaga, N., et al. 2015, *ApJ*, **814**, 29
- Katz, B., & Waxman, E. 2008, *JCAP*, **01**, 018
- Kishishita, T., Hiraga, J., & Uchiyama, Y. 2013, *A&A*, **551**, 132
- Knödolseder, J., Mayer, M., Deil, C., et al. 2013, Proc. 33rd ICRC, 00772
- Knödolseder, J., Mayer, M., Deil, C., et al. 2016, *A&A*, **593**, A1
- Koyama, K., Kinugasa, K., Matsuzaki, K., et al. 1997, *PASJ*, **49**, L7
- Koyama, K., Petre, R., Gotthelf, E. V., et al. 1995, *Natur*, **378**, 255
- Lazendic, J. S., Slane, P. O., Gaensler, B. M., et al. 2003, *ApJL*, **593**, L27
- Lee, S.-H., Ellison, D. C., & Nagataki, S. 2012, *ApJ*, **750**, 156
- Lee, S.-H., Patnaude, D. J., Raymond, J. C., et al. 2015, *ApJ*, **806**, 71
- Lee, S.-H., Slane, P. O., Ellison, D. C., Nagataki, S., & Patnaude, D. J. 2013, *ApJ*, **767**, 20
- Longair, M. S. 1994, *High Energy Astrophysics, Vol. 2, Stars, the Galaxy and the Interstellar Medium* (Cambridge: Cambridge Univ. Press)
- Malkov, E., & Drury, L. O. 'C. 2001, *RPPH*, **64**, 429
- Malkov, M. A. 1997, *ApJ*, **485**, 638
- Malkov, M. A., Diamond, P. H., Sagdeev, R. Z., Aharonian, F. A., & Moskalenko, I. V. 2013, *ApJ*, **768**, 73
- Marcowith, A., & Casse, F. 2010, *A&A*, **515**, A90
- Mattox, J. R., Bertsch, D. L., Chiang, J., et al. 1996, *ApJ*, **461**, 396
- Maxted, N. I., Rowell, G. P., Dawson, B. R., et al. 2012, *MNRAS*, **422**, 2230
- Moriguchi, Y., Tamura, K., Tawara, Y., et al. 2005, *ApJ*, **631**, 947
- Morlino, G., Amato, E., & Blasi, P. 2009, *MNRAS*, **392**, 240
- Morlino, G., Blasi, P., Bandiera, R., Amato, E., & Caprioli, D. 2013, *ApJ*, **768**, 148
- Muraishi, H., Tanimori, T., Yanagita, S., et al. 2000, *A&A*, **354**, L57
- Ohira, Y. 2012, *ApJ*, **758**, 97
- Ohira, Y., Murase, K., & Yamazaki, R. 2010, *A&A*, **513**, A17
- Ohira, Y., Murase, K., & Yamazaki, R. 2011, *MNRAS*, **410**, 1577
- Ohira, Y., Terasawa, T., & Takahara, F. 2009, *ApJL*, **703**, L59
- Ohira, Y., Yamazaki, R., Kawanaka, N., & Ioka, K. 2012, *MNRAS*, **427**, 91
- Parizot, E., Marcowith, A., Ballet, J., & Gallant, Y. A. 2006, *A&A*, **453**, 387
- Pohl, M., Yan, H., & Lazarian, A. 2005, *ApJL*, **626**, L101
- Protassov, R., van Dyk, D. A., Connors, A., Kashyap, V. L., & Siemiginowska, A. 2002, *ApJ*, **571**, 545
- Ptuskin, V. S., & Zirakashvili, V. N. 2003, *ApJ*, **403**, 1
- Ptuskin, V. S., & Zirakashvili, V. N. 2005, *A&A*, **429**, 755
- Sano, H., Fukuda, T., Yoshiike, S., et al. 2015, *ApJ*, **799**, 175
- Sano, H., Sato, J., Horachi, H., et al. 2010, *ApJ*, **724**, 59
- Sano, H., Tanaka, T., Torii, K., et al. 2013, *ApJ*, **778**, 59
- Slane, P., Gaensler, B. M., Dame, T. M., et al. 1999, *ApJ*, **525**, 357
- Tanaka, T., Uchiyama, Y., Aharonian, F. A., et al. 2008, *ApJ*, **685**, 988
- Tsunemi, H., Miyata, E., Aschenbach, B., Hiraga, J., & Akutsu, D. 2000, *PASJ*, **52**, 887
- Uchiyama, Y., Aharonian, F. A., & Takahashi, T. 2003, *A&A*, **400**, 567
- Uchiyama, Y., Aharonian, F. A., Tanaka, T., Takahashi, T., & Maeda, Y. 2007, *Natur*, **449**, 576
- Uchiyama, Y., Blandford, R. D., Funk, S., Tajima, H., & Tanaka, T. 2010, *ApJL*, **723**, L122
- Vink, J., & Laming, J. M. 2003, *ApJ*, **584**, 758
- Völk, H. J., Berezko, E. G., & Ksenofontov, L. T. 2005, *A&A*, **433**, 229
- Wang, A.-R., Qu, Q.-Y., & Chen, Y. 1997, *A&A*, **318**, L59
- Warren, J. S., Hughes, J. P., Badenes, C., et al. 2005, *ApJ*, **634**, 376
- Wilks, S. S. 1938, *Ann. Math. Statist.*, **9**, 60
- Yamazaki, R., Kohri, K., & Katagiri, H. 2009, *A&A*, **495**, 9
- Yan, H., Lazarian, A., & Schlickeiser, R. 2012, *ApJ*, **745**, 140
- Zirakashvili, V. N., & Aharonian, F. A. 2010, *ApJ*, **708**, 965